Mechanical model based on a BVP for FRPs applied on flat and curved masonry pillars with anchor spikes

Elisa BERTOLESI* [(1)], Ernesto GRANDE[(2)], Mario FAGONE[(3)], Gabriele MILANI[(4)], Tommaso ROTUNNO[(5)]

(1) *College of Engineering, Design and Physical Sciences, Brunel University London, Howell Building 236, Kingston Lane, Uxbridge, Middlesex UB8 3PH, UK*

(2) *Department of Sustainability Engineering, University Guglielmo Marconi, Via Plinio 44, 00193 Rome (Italy)*

(3) *Dipartimento di Ingegneria Civile e Ambientale (DICEA), Università degli Studi di Firenze, Piazza Brunelleschi 6, 50121 Florence (Italy)*

(4) *Department of Architecture, Built environment and Construction engineering (ABC), Politecnico di Milano, Piazza Leonardo da Vinci 32, 20133, Milan (Italy)*

(5) *Dipartimento di Architettura (DiDA), Università degli Studi di Firenze, Piazza Brunelleschi 6, 50121 Florence (Italy)*

* corresponding author, e-mail: elisa.bertolesi@brunel.ac.uk

Abstract

The use of fiber reinforced polymer (FRP) materials for strengthening interventions of existing constructions is a consolidated and widespread technique. In this context, although strengthening interventions generally involve curved masonry elements (arches, vaults, domes, etc.), only a few studies specifically concern the influence of the geometry curvature, or the effect of mechanical anchors (widely used in current practice for preventing premature failures), on the bond behavior of FRPs. The present paper proposes an interface exponential model for simulating the bond behavior of curved masonry pillars reinforced with FRP strips applied at the intrados or extrados by both epoxy adhesive and anchor spikes. The proposed model is based on a relatively simple boundary value problem (BVP) obtained by assuming for the spike a constitutive behavior under shear forces quantitatively deduced by post-processing the numerical data from a finite element micro-modeling approach previously proposed by the authors. The application of the proposed model to experimental cases carried out by the authors underline the stability of solution and the reliability of the proposed approach to account for the effect of both the curvature of the substrate and presence of the spike anchor on the bond behavior of FRPs.

Keywords: masonry; arches and vaults; CFRP reinforcement; anchor spike; non-linear Boundary Value Problem for ODEs; debonding.

1. Introduction

The preservation of the masonry-built heritage is nowadays considered a priority in highly civilized countries. Among the different typologies of masonry structural elements that the scientific community is trying to preserve against extreme events like earthquakes floods and storms, the most diffused is probably constituted by curved structures, such as arches, vaults, domes, etc..

Masonry behavior is well known for its main weakness in tension, exhibiting such kind of material a very limited tensile strength with marked softening, an almost cohesiveness frictional behavior and a fairly good resistance in compression, followed by a mild softening with good dissipation in terms of inelastic energy for crushing.

As a natural consequence of such kind of behavior, for arches and curved structural elements in general, it appears very suitable to insert in all those zones undergoing tensions, strengthening elements capable to absorb tensile stresses that otherwise would result into the propagation of flexural cracks, up to the formation of a failure mechanism which usually appears at early stages of the application of the horizontal loads.

For this reason, gluing FRP strips on the surface of such kind of structures appears an extremely interesting technology that deserves to be studies [1–6].

In general, at present, the literature in the field of FRP strengthening on masonry surfaces results superabundant both from an experimental and numerical point of view [7,8,17–26,9,27–30,10–16], having also at disposal a variety of technical recommendations especially useful for practitioners involved in such kind of structural upgrading [31].

However, the studies on curved masonry substrates appear still relatively limited and recommendations given by codes of practice are rather vague in this regard, leaving space for further research in this field, both experimental and numerical [26-47].

In particular, it is still not very clear and quantitatively determined the role played by anchorage devices applied near the free edges of a reinforcement.

The present paper moves its step from a previous combined experimental and numerical research made on curved pillars reinforced with FRP and subjected to standard debonding tests, in presence or absence of anchor spikes [43–46,48–53]. The main aim was to provide information on the ultimate load carrying capacity and ductility of such kind of reinforcement when subjected to standard debonding and to compare the global and local results maintaining the same geometries and materials used in presence and absence of anchorage.

The paper here presented proposes an interface exponential model for masonry pillars reinforced with FRP strips where the material properties of the interface are calibrated by best fitting of the previously obtained experimental results. The presence of the anchor spike is modeled by assuming for the spike a constitutive behavior under shear forces which is quantitatively deduced from post processing of numerical data obtained by a previous research by the authors, where the debonding process was modelled in ABAQUS FEM software assuming damage propagating in the bulk substrate [44,52].

A relatively simple Boundary Value Problem (BVP) is obtained, where the presence of a concentrated load in correspondence of the spike is dealt with a suitable and robust approach where the concentrated load is substituted by a distributed tangential stress with equivalent properties.

A standard BVP solver based on finite difference is adopted, which showed excellent numerical stability and efficiently in all the cases investigated.

Three different sets of mechanical properties are considered for the FRP/substrate interface and the spike constitutive behavior. The first two models (called Set 1 and Set 3) assumes two interface relationships formally equivalent to the data reported in Bertolesi and co-workers in [52] where damage in the bulk was considered with different fracture energies in tension and compression for bricks and mortar. The third model assumes for the interface Set 1 data and for the spike constitutive behavior the trilinear relationship proposed by Grande et al. in [48], which turns out to be independent from the curvature of the substrate.

In all cases, excellent agreement with experimental data and previously presented numerical models is found [48,52], showing that the present simple approach can be used by any practitioner for a fast and reliable prediction of the debonding behavior of FRP on masonry curved structures in presence of anchor spikes. Finally, the role played by the spike is clearly reproduced by the procedure here proposed, where it is underlined an evident activation at a relatively advanced state of deformation.

2. Brief overview of the experimentation carried out

A brief summary of the experimental study published in [46] is given below. The reader can refer to the cited paper for further details. The experimental program involved twenty-five specimens, subdivided into five series: CA-I-A, CA-E-A, CB-I-A, CB-E-A, C0-A; the first four series refer to curved specimens while the last refers to flat specimens. Two different radii of curvature (R = 1500 mm, referred to as "CA" and R = 3000 mm, referred to as "CB") were considered in order to study the behavior of the specimens in various geometric conditions.

All specimens were reinforced with a CFRP strip and equipped with a single anchor spike (referred to as “-A” in the specimen’s labelling). Some of the curved specimens were reinforced at the intrados (labeled with “I”) and the others at the extrados (labeled with “E”). All the specimens were made of five bricks (dimensions 65x120x250 mm^3) by interposed four mortar joints of constant thickness in flat specimens and variable thickness in curved specimens (minimum thickness 10 mm), as shown in Figure 1.

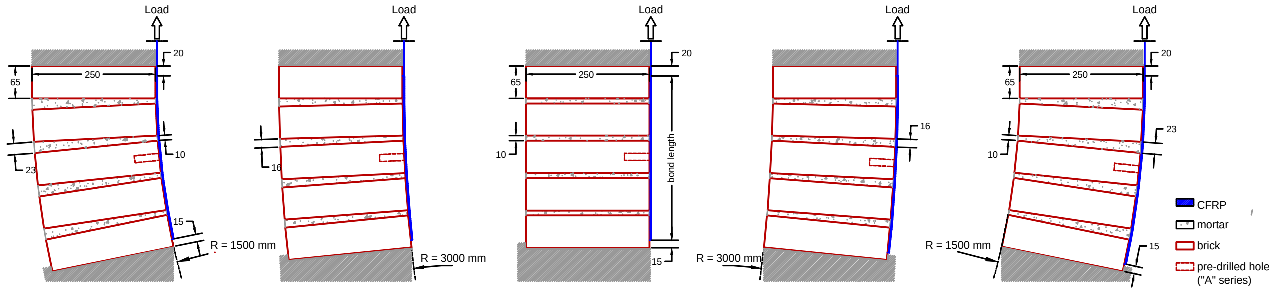

L_{CAI}= 330 mm L_{CBI}= 330 mm L_{Flat}= 330 mm L_{CBE}= 354 mm L_{CAE}= 382 mm

Figure 1: The five series of experimentally tested FRP reinforced curved and flat masonry pillars.

The carbon fiber fabric sheet used to manufacture the specimens had a nominal thickness of 0.165 mm (as declared by the supplier), a width of 100 mm and a length ranging from 330 mm to 382 mm according to the geometry of the surface to be bonded. Only a part of the sheet was bonded to the masonry, one part remained dry and the end part was glued to the steel loading device of the test machine. The length glued to the brick (L) is variable according to the geometry of the specimen (Figure 1) but is always greater than the effective bonding length (L_{eff}=122mm), calculated with the formula provided by CNR-DT200 [31] with reference to flat configurations.

The mechanical properties of the materials composing the reinforcement, declared by the manufacturer, are reported in Table 1 and those of the brick and mortar, obtained from an experimental investigation [46,51], are reported in Table 2.

Table 1: Mechanical properties of the reinforcing system components (declared by the manufacturer).

	Nominal thickness [mm]	Tensile elastic modulus [MPa]	Bending elastic modulus [MPa]	Ultimate tensile strain [%]	Characte-ristic tensile strength [MPa]	Shear strength [MPa]
Unidirectiona l carbon fiber fabric	0.165	240000	--	1.3	3200	--
Adhesive	--	--	2200	--	--	95

Table 2: Mechanical properties of the bricks and mortar.

	n. specimens	Mean [MPa]	C.V. [%]
CLAY BRICK			
Compressive strength	6	19.90	5.11
Young modulus	6	8712	6.92
Direct tensile strength	6	2.49	16.90
Bending tensile strength	6	3.36	33.77
MORTAR			
Bending tensile strength	6	1.85	9.42
Compressive strength	12	5.18	8.212

In all the specimens, the CFRP sheets were equipped with an anchor spike, also in CFRP, inserted at center of the central brick. The anchor was made by rolling up a rectangle (200x90 mm^2) of carbon fiber fabric sheet. Before being rolled up, a part of the fabric measuring 35x200 mm^2 was pre-impregnated with resin. Thus, the cylinder obtained was inserted partly (impregnated portion) into a hole drilled in the center of the central brick and partly (dry portion) layered and fan-glued onto the carbon strip, as shown in Figure 2 [46].

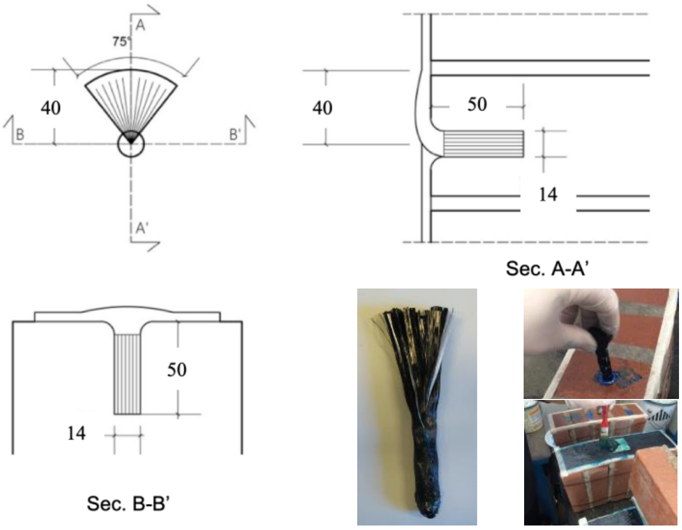

Figure 2: Spike anchors: geometric characteristics (measures in mm) [46].

All the specimens were subjected to a single lap shear test: the masonry pillars were constrained by two steel plates and the force was applied to the end of the carbon sheet (see Figure 3).

The tests were carried out under displacement control; the displacement was increased monotonically by means of an actuator equipped with a fork and a steel cylinder, to which the end of the carbon fiber fabric sheet was glued.

The specimens were equipped with a load cell (50 kN), two “omega” transducers (“O1” and “O2”), four displacement transducers (“TL”, “TR”, “T1” and “T2”) and two strain gauges (“SG01” and “SG02”, applied to three specimens of each series) as showed in Figure 3.

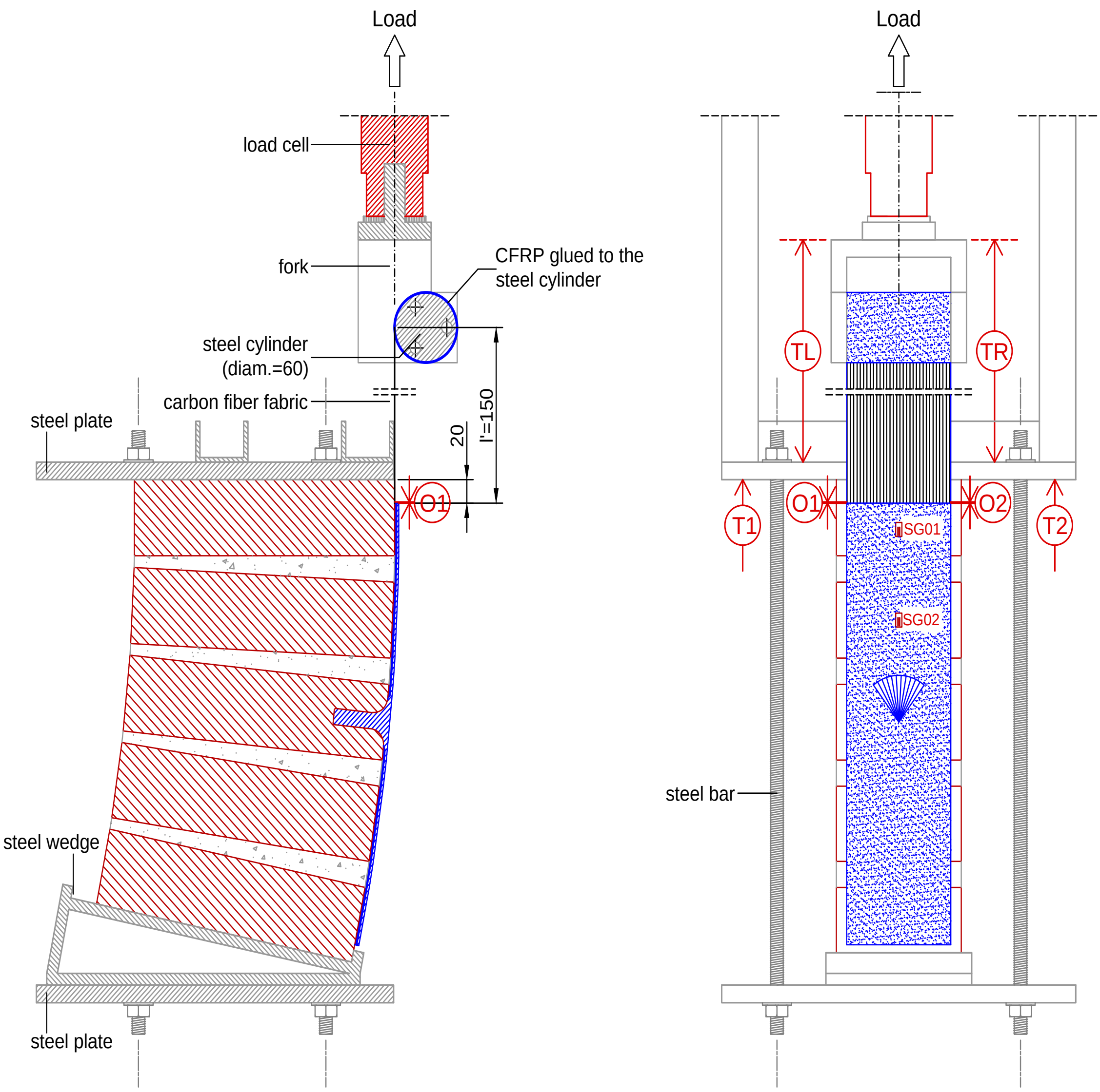

Figure 3: Test setup and instrumentation.

The overall behavior of the specimens can be described by analyzing the load-slip diagrams shown in Figure 4, where $\bar{s}$ in abscissa represents the sliding between the upper end (loaded side) of the reinforcement and the masonry substrate. All the load-slip diagrams present a quasi-linear initial branch, ending with the formation of the first cracks in the masonry substrate, near the loaded end of the reinforcement (i.e. far from the anchor). After that, the diagrams show a load drop and a subsequent ascending branch, much more scattered than the first one, until the maximum load is reached. Then, the diagrams referring to flat specimens and to curved specimens reinforced at the intrados show a sudden load decrease and a final post-peak branch corresponding to an average load of about 30% to 55% (depending on the series) of the maximum load. The specimens of such series mainly showed a cohesive failure mode, corresponding to the detachment of the CFRP sheet because of fractures occurring in the substrate, a few millimeters below the composite reinforcement, associated to the pull out of the anchor spike.

Differently, the diagrams referring to the curved specimens reinforced at the extrados show a different behavior: these, in fact, exhibited a brittle failure mode occurring because of the tensile failure of the dry carbon fiber fabric, outside the bonded zone. In this case, in fact, the anchor and the stabilizing effect of the curvature prevented the detachment of the CFRP sheet reinforcement during the test. It should however be noted that the average value of the maximum load of the specimens reinforced at the extrados corresponds to about 50% of the nominal capacity of the dry fabric declared by the manufacturer (see Table 3). This is due to a not perfectly uniform distribution of the load in the dry fabric during the test.

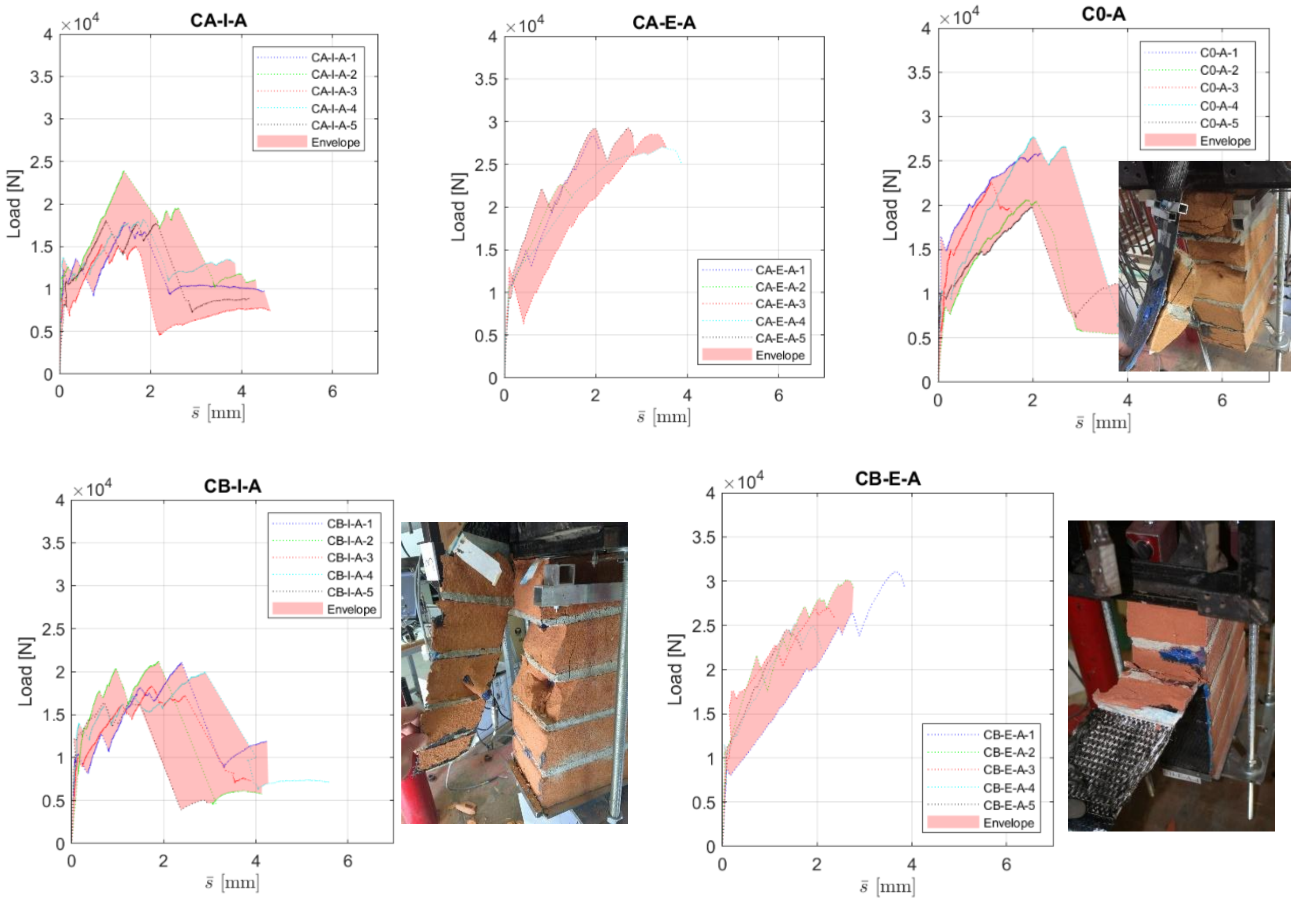

Figure 4: Experimental load-slip diagrams (slip $\bar{s}$ refers to the loaded end of the reinforcement).

2.1. Characterization of the CFRP-to-masonry interface

The deformation values measured by the strain gauges externally glued to the reinforcement (SG01 and SG02 in Figure 3) were used to experimentally investigate the stress-slip behavior of the interface between the reinforcement and the substrate. Indeed, considering the schematization of the portion of reinforcement between SG01 and SG02 (see Figure 5), the average shear interface stress ($\bar{\tau}_{1-2}$) and normal reinforcement stress ($\bar{\sigma}_{1-2}$) components were evaluated enforcing simple equilibrium conditions through the following formulas:

$$\bar{\tau}_{1-2} = \frac{E_F(\varepsilon_1 - \varepsilon_2)\, t_F \cos\alpha}{\Delta x} \tag{1}$$

$$\bar{\sigma}_{1-2} = \frac{E_F(\varepsilon_1 + \varepsilon_2)\, t_F \sin\alpha}{\Delta x} \tag{2}$$

being:

E_F = (homogenized) elastic modulus of the composite reinforcement in the fiber direction

ε_1 e ε_2 = strain values measured with SG01 and SG02 respectively

t_F = thickness of the strengthening material (1 mm)

α and Δx = inclination of the reinforcement due to the curvature and distance between the two strain gauges respectively

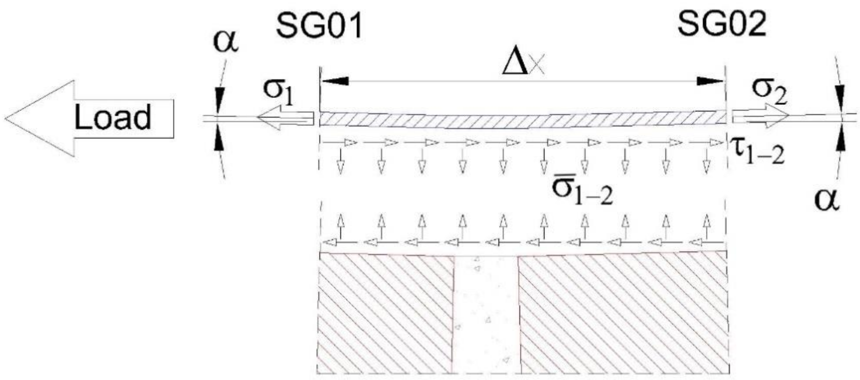

Figure 5: Scheme of the stress distribution at the reinforcement-masonry interface between SG01 and SG02.

Of course, normal stresses are negative (compressive) in the case of reinforcements bonded at the extrados, positive (tensile) in the case of reinforcements bonded at the intrados and zero in the case of flat specimens. The interface stress values referring to the portion of reinforcement between SG02 and the anchor spike were evaluated using relations analogous to (1-2) assuming that the deformation ε at the anchor was zero.

The slip values s_1 and s_2 corresponding respectively to the position of the strain gauges SG01 and SG02 were evaluated assuming a linear deformation field between the two strain gauges and between the anchor and SG02 and, in addition, that no slip occurred at the anchor. This last hypothesis seems to be acceptable at least in the pre-peak phases of the tests, but it could lead to not negligible errors in the final part, when the specimens are more damaged. For this reason, the data corresponding to the last part of the tests were not considered for the evaluation of the slip and, therefore, of the average interface stress components.

In agreement with the previously described hypotheses, it is easily calculated both the slips at the strain gauges location:

$$s_2 = \frac{\varepsilon_2 \Delta x}{2} \qquad (3)$$

$$s_1 = s_2 + \frac{(\varepsilon_1 + \varepsilon_2)\Delta x}{2} \tag{4}$$

and so, the average slip values between SG01 and SG02 ($\bar{s}_{1-2}$) and between SG02 and the anchor ($\bar{s}_{2-A}$) have been evaluated as

$$\bar{s}_{1-2} = \frac{s_1 + s_2}{2} \tag{5}$$

$$\bar{s}_{2-A} = \frac{s_2}{2} \tag{6}$$

Shear stress-slip values obtained as described are represented in Figure 6, whilst in Figure 7 are reported the results in terms of normal stress-slip values. These results underline a good agreement with the analogous diagrams obtained by the Authors using the same procedure with reference to not anchored reinforcements [44,45,51]. Shear stress-slip diagrams of the non-anchored flat series (C0-0) have also been reported in Figure 6. Such diagrams have been obtained using five strain gauges, differently from C0-A series where only two strain gauges could be used. Therefore, since τ-slip experimental values corresponding to C0-0 series refer to a longer part of the reinforcement, these were considered suitable to calibrate the interface constitutive law as described below.

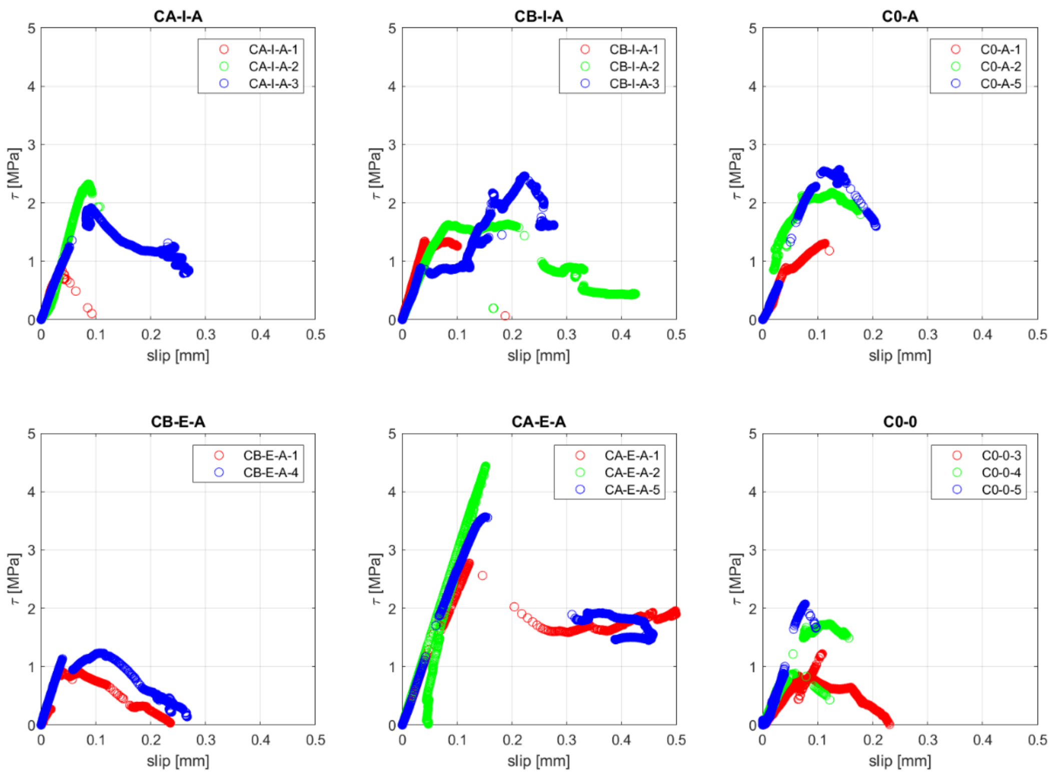

Figure 6: Experimental τ-slip diagrams in presence of anchorage and without anchorage for only C0-0 series (flat case without anchorage).

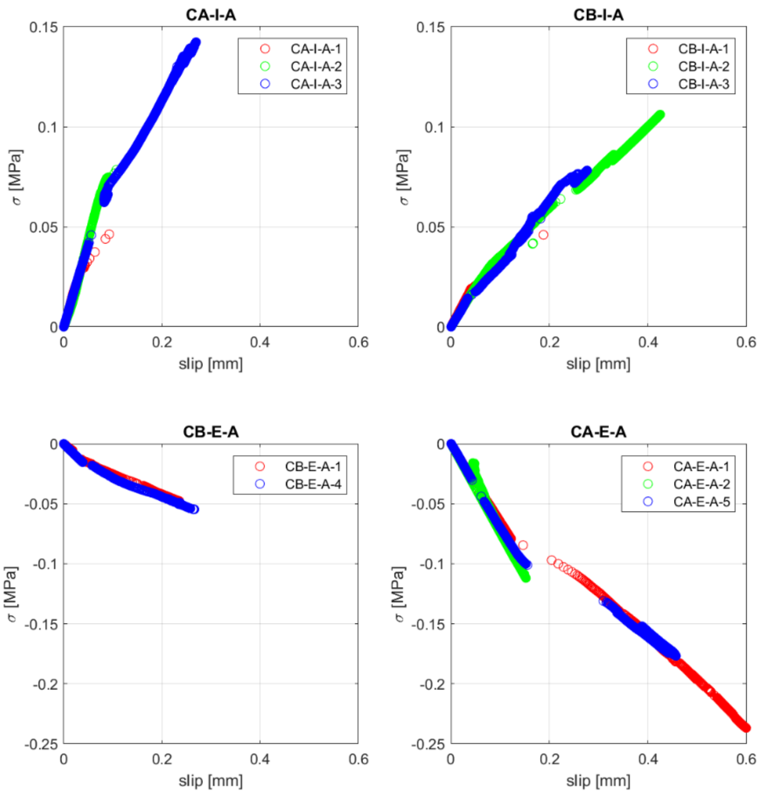

Figure 7: Experimental σ-slip diagrams.

3. The mathematical model in brief

The mathematical model adopted in the computations presented in this paper is identical to that proposed by the authors for the same specimens without anchor spikes, see [54]. The novelty here relies on how the anchor spike is taken into account.

For the flat case without anchor spike, the Boundary Value Problem BVP which solves the delamination problems is the following:

$$t_F E_F \frac{d^2 s}{dx^2} - \tau(s,x) = 0 \qquad \left.\frac{ds}{dx}\right|_{x=0} = 0 \qquad s|_{x=L_F} = \bar{s}_0 \tag{7}$$

where t_F and E_F are FRP thickness and its Young Modulus, respectively, s is the slip between FRP and substrate, x indicates the abscissa of a point of the FRP/substrate interface having defined the free edge of the FRP strip as the origin of the frame of reference, $\tau(s,x)$ is the tangential stress field acting at the FRP/substrate interface and L_F is the fiber bonded length; $\bar{s}_0$ is the slip at the loaded end.

When an anchor spike of diameter d_s is connected to the support at a distance L_S from the x frame of reference origin, the same BVP of Eq. (7) must be solved, exception made that a fictitious tangential stress $\tau^*(s,x)$ is taken into account instead of $\tau(s,x)$ for all those points with abscissa x_p laying within the interval $L_S - \frac{d_s}{2} \leq x_p \leq L_S + \frac{d_s}{2}$.

$\tau^*(s,x)$ is evaluated knowing the force $F_s(s_s, L_s)$ acting on the spike in correspondence of a slip in the spike equal to s_s according to the following formula:

$$\tau^*(s,x) = \frac{F_s(s_s, L_s)}{B_F d_s} \qquad (8)$$

where B_F it is FRP width.

It is worth mentioning that Eq. (8) is not easy to be solved numerically, because the computation of τ^* requires the knowledge of the slip in another position, albeit very near, i.e. that of the spike. However, assuming the dimension of the spike negligible when compared to the overall dimension of the glued length, it is possible to assume $s \equiv s_s$. Authors experienced that if the interval length where τ^* replaces τ is small enough (up to 2 times the diameter of the spike in the present simulations, i.e. up to roughly 1% of the length of the reinforcement), negligible differences in terms of global response are obtained among different choices of the length. On the other hand, very small values of the interval length lead to computational efforts of the BVP solver that grow exponentially. For this reason, a length equal to the diameter of the spike is adopted in the present simulations, thus obtaining a good balance between computational burden and reliability of the solver and, at the same time, maintaining geometrical consistency with the experimentation carried out.

As far as the curved cases without anchor spike are concerned, the Boundary Value Problem BVP which governs the delamination problem is the following:

$$t_F E_F \frac{d^2 s}{dx^2} - \tau(s, x, \sigma_n) = 0 \qquad \left.\frac{ds}{dx}\right|_{x=0} = 0 \qquad s|_{x=L_F} = \bar{s}_0$$
$$\sigma_n = \frac{t_F E_F}{R}\frac{ds}{dx} \qquad (9)$$

In Eq. (9), it is evident how the presence of a normal stress σ_n at the FRP/substrate modifies the BVP of the flat case only in the evaluation of tangential stresses τ, which typically follow a Mohr-Coulomb behavior, changing both peak strength and ultimate ductility depending if σ_n is positive or negative.

The presence of the anchor spike is managed exactly in the same way briefly discussed for the flat case. In absence of a comprehensive experimental characterization of the anchor spike behavior in presence of a tangential load (increase up to failure) and a constant normal stress to apply at the head of the spike, the constitutive behavior of the spike $F_s(s_s, L_s)$ is derived by post-processing the Abaqus simulations reported in [52], as it will be discussed later on.

The $\tau(s, x, \sigma_n)$ constitutive relationship assumed for the FRP/substrate interface is the following:

$$\tau(s) = (\tau_M - \tau^*)\frac{s}{s_0}e^{\frac{\rho}{2}\left[1-\left(\frac{s}{s_0}\right)^2\right]} + \tau_r\left[1 - e^{-\frac{\rho}{2}\left(\frac{s}{s_0}\right)^2}\right] \qquad (10)$$

In Eq. (10), the symbols have the following meaning: τ_M and τ_r are the peak and residual stress, ρ is a non-dimensional parameter tuning softening (or alternatively fracture energy) and s_0 the slip at $\tau = (\tau_M - \tau^*)$. τ^* is a further stress constant value that tunes that the maximum stress τ_M occurs at a slip equal to s^*.

It can be easily shown that s^* is obtained as follows:

$$s^* = \frac{\tau_r\rho + \sqrt{(\tau_r\rho)^2 + 4\rho\left[(\tau_M - \tau^*)e^{\frac{\rho}{2}}\right]^2}}{2\rho(\tau_M - \tau^*)e^{\frac{\rho}{2}}}s_0 \qquad (11)$$

According to [54], τ^* and s^* are obtained intersecting the following two functions:

$$\begin{aligned} f_1(s^*) \rightarrow \quad & \tau^* = \tau_M - \frac{\tau_M - \tau_r\left[1 - e^{-\frac{\rho}{2}\left(\frac{s^*}{s_0}\right)^2}\right]}{\frac{s^*}{s_0}e^{\frac{\rho}{2}\left[1-\left(\frac{s^*}{s_0}\right)^2\right]}} \\ f_2(s^*) \rightarrow \quad & \tau^* = \tau_M - \frac{\tau_r}{e^{\frac{\rho}{2}}\left(\frac{s^*}{s_0} - \frac{1}{\rho\frac{s^*}{s_0}}\right)} \end{aligned} \qquad (12)$$

A normal stress σ_n acting at the FRP/substrate inteface modifies τ_M, s_0 and τ_r according to a Mohr-Coulomb relationship as follows:

$$\tau_M^* = \tau_M - \sigma_n \tan\Phi \quad s_0^* = \frac{\tau_M^*}{\tau_M}s_0 \quad \begin{cases} \tau_r^* = \tau_r - \sigma_n \tan\Phi & \sigma_n < 0 \\ \tau_r^* = 0 & \sigma_n \geq 0 \end{cases} \qquad (13)$$

In practice, Eq. (13) replaces τ, s, τ_r with τ_r^*, s^*, τ_r^* in Eq. (10) when the normal stress at the interface is not zero.

It is interesting to point out how, from Eq. (13), slip s_0 varies linearly with τ_M^*, which is indeed a variation of the ductility which indirectly utilizes a Mohr-Coulomb failure criterion. As well known, indeed, displacements are independent from cohesive-frictional relationships, which refer exclusively to ultimate strengths. As a matter of fact, ruling slip parameter with the ratio $\frac{\tau_M^*}{\tau_M}$ transfers on displacements the linear relationship adopted for stresses, which in this case is cohesive-frictional. Such approach was proved to be in agreement with the actual behavior of the FRP/substrate interface also as far as displacements are concerned, because ductility is increased linearly with σ_n according to a Mohr-Coulomb criterion.

$\tau(s)$ and $\tau^*(s)$ relationships can be suitably determined by means of numerical least-squares procedures where a best fitting of experimental data is performed, once the information provided by strain-gauges installed (if any) on the surface of the FRP strip is available.

As already discussed in the previous section, installing some strain gauges on the FRP surface allows to experimentally determine directly local strains of the fiber, say $\varepsilon_{F,SGi}$ on the i-th strain gauge SG, and hence indirectly the experimental $\tau(s) - s$ relationship to adopt.

The results of the non-linear best fitting have been already presented in [44,52], where the reader is referred. Here, we present only the obtained numerical parameters for the different coefficients τ_M, τ_r, s_0, ρ and Φ (see Table 3) characterizing the $\tau(s)$ and its shape at $\sigma_n = 0; \pm 0.1; \pm 0.5\ MPa$, which correspond roughly to the flat case, CAI & CAE and CBI & CBE. The different curves are depicted in Figure 8 and they are compared with the bilinear relationships (which obey a Mohr-Coulomb failure criterion in the same way the present approach does) adopted by Grande and co-workers in [49].

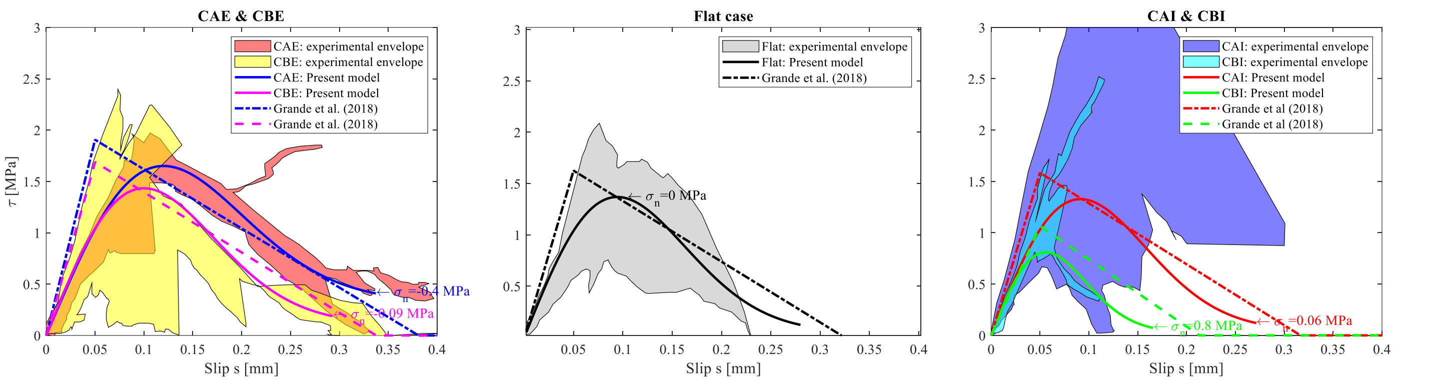

-a -b -c

Figure 8: Interface τ -slip behavior assumed in the simulations and comparison with an existing bilinear relationship. -a: CAE &CBE. -b: Flat. -c: CAI & CBI

Table 3: Parameters adopted to characterize the interface behavior by means of non-linear least squares optimization (corresponding to Set 1 mechanical properties adopted in [52]).

τ_M	τ_r	s_0	ρ	Φ
MPa	MPa	mm	-	°
1.42	0.02	0.031	0.088	35

It is also necessary to say a few words about the constitutive behavior to utilize for spike in the numerical simulations. First of all, it should be pointed out that only the shear behavior is required, according to Eqs. (7)(8). At present, it is still under study by the authors a comprehensive experimental campaign aimed at determining the constitute behavior of the spike, also in presence of different values of normal stress σ_n, in the range observed for CAI & CAE. However, in absence of such results, here the 3D Abaqus models used to analyze the pillars reinforced with FRP and anchor spike already presented in [52], are re-considered to find, through suitable post processing of the numerical results, the spike constitutive behavior provided by that models in terms of tangential force of the spike and slip of the point of application of the spike, i.e. $F_s - s_s$ relationship.

Indeed, the constitutive behavior of the spike anchor (i.e. $F_s - s_s$ relationship) can be extracted by considering that the external load applied to the FRP strip is transferred to the spike anchor inserted into the masonry pillar by a small area (i.e. red area depicted in Figure 9) connecting the external fan to the FRP anchor. Thus, $F_s - s_s$ relationship representing the spike behavior are obtained by trivial integration of the stresses on such section at different loading steps i:

$$F_s = \sum \sigma_i B_i t_i \qquad (14)$$

Where σ_i is the vertical stress at node i acting on sections I, while $B_i * t_i$ is the influence area of node i located on the section (red area) depicted in Figure 9. Summation bounds and B_i depended on the FE mesh which in turn depends on the pillar geometry, whereas t_i was assumed equal to the FRP thickness. The slip $s_s$was obtained averaging the displacement monitored in each node of section I.

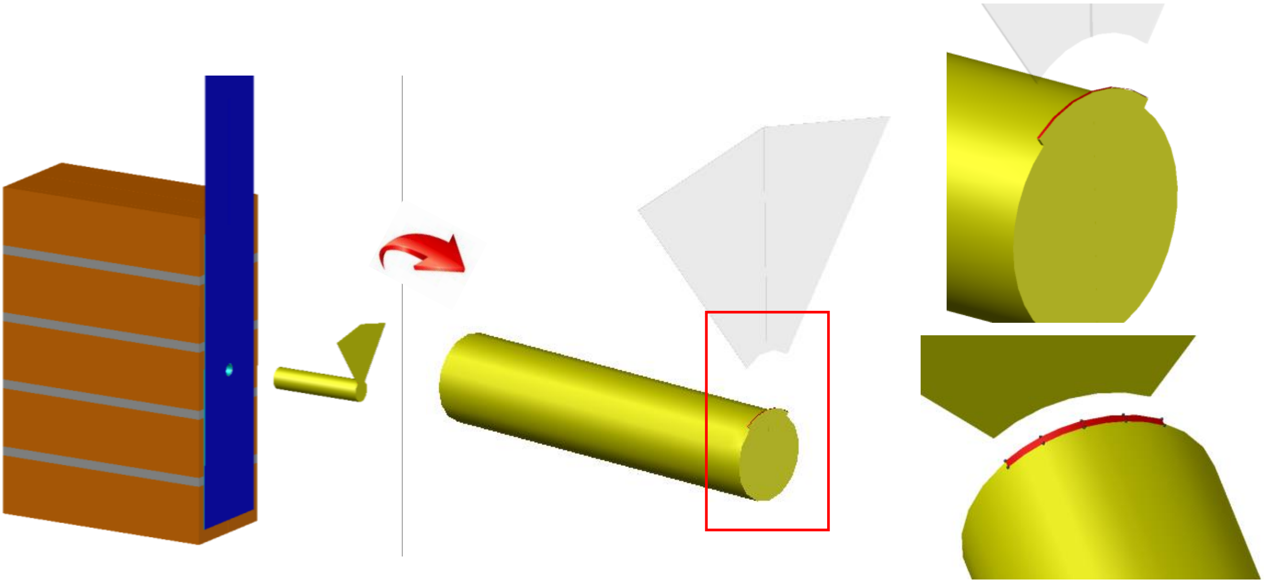

Figure 9: Post processing on Abaqus 3D FE models with spike to numerically deduce the spike constitutive behavior.

Applying the aforementioned procedure, $F_s - s_s$ relationships depicted in Figure 10 for the different cases are obtained. Only results for the Flat, CAE and CAI models are represented for the sake of conciseness. As it can be observed, in the Abaqus model proposed in [52], 3 different sets of mechanical properties are assumed for bricks and mortar, called Set 1, Set 2 and Set 3, see Figure 11-a & -b. In the numerical applications here proposed, only Set 1 and Set 3 are taken into consideration, providing Set 2 intermediate results between the aforementioned ones. The three Sets of mechanical properties considered in [52] differ only for the fracture energies and the post-peak behavior adopted for the constituent materials. The remaining mechanical properties adopted correspond all to those experimentally evaluated in [46,51] (e.g. peak strength and elastic moduli). The behavior of the interface between FRP and substrate adopted here (see Table 3) is assumed in agreement to an experimental data fitting in absence of anchor spike, as discussed in detail in [44]. Such approach does not have a direct link with the approach proposed in [44] for Set 1 and Set 3, but according to the results obtained, it may be considered reasonable to associate Set 1 experimental data with the interface model of Table 3, since Set 1 data in [44] exhibit the best agreement with experimental global displacement curves. In order to find interface model parameters corresponding to Set 3, it may seem reasonable to proceed in terms of fracture energies. Consistently with such assumption, a new interface model is also used here which should correspond to Set 3 experimental data, assuming for the exponential model of Eq. (10) the needed parameters in terms of fracture energy. Let us assume that the fracture energies in compression and tension for bricks in the model proposed in [44] are $\Gamma_{bc,3}$, $\Gamma_{bt,3}$ for Set 3 and $\Gamma_{bc,1}$, $\Gamma_{bt,1}$ for Set 1. Their ratios ($\Gamma_{bc,3}/\Gamma_{bc,1}$ and $\Gamma_{bt,3}/\Gamma_{bt,1}$) turn out to be respectively equal to 3.02 and 0.88

respectively. It is assumed that for the interface model fracture energies corresponding to the Set 3 and Set 1 data are equal to $\Gamma_{bI,3}$ and $\Gamma_{bI,1}$. Their ratio $\Gamma_{bI,3}/\Gamma_{bI,1}$ is equated to $\sqrt{\Gamma_{bc,3}\Gamma_{bt,3}/(\Gamma_{bc,1}\Gamma_{bt,1})}$, an assumption which allows to evaluate $\Gamma_{bI,3}$ and hence the corresponding interface law, which should represent Set 3 data reported in [44]. The resulting parameters are summarized in **Error! Reference source not found.** and the corresponding curve in absence of normal stresses is shown in Figure 11-c, where also experimental data collected in absence of the anchor spike are also represented with the trilinear law adopted in Grande et al. [49]. As it can be noticed, the experimental data fitting is satisfactory also in this second case, meaning that all data-sets assumed in [52] seem reasonable to describe the experimental behavior of the debonding problem, assuming exclusively damage in the bulk of the substrate.

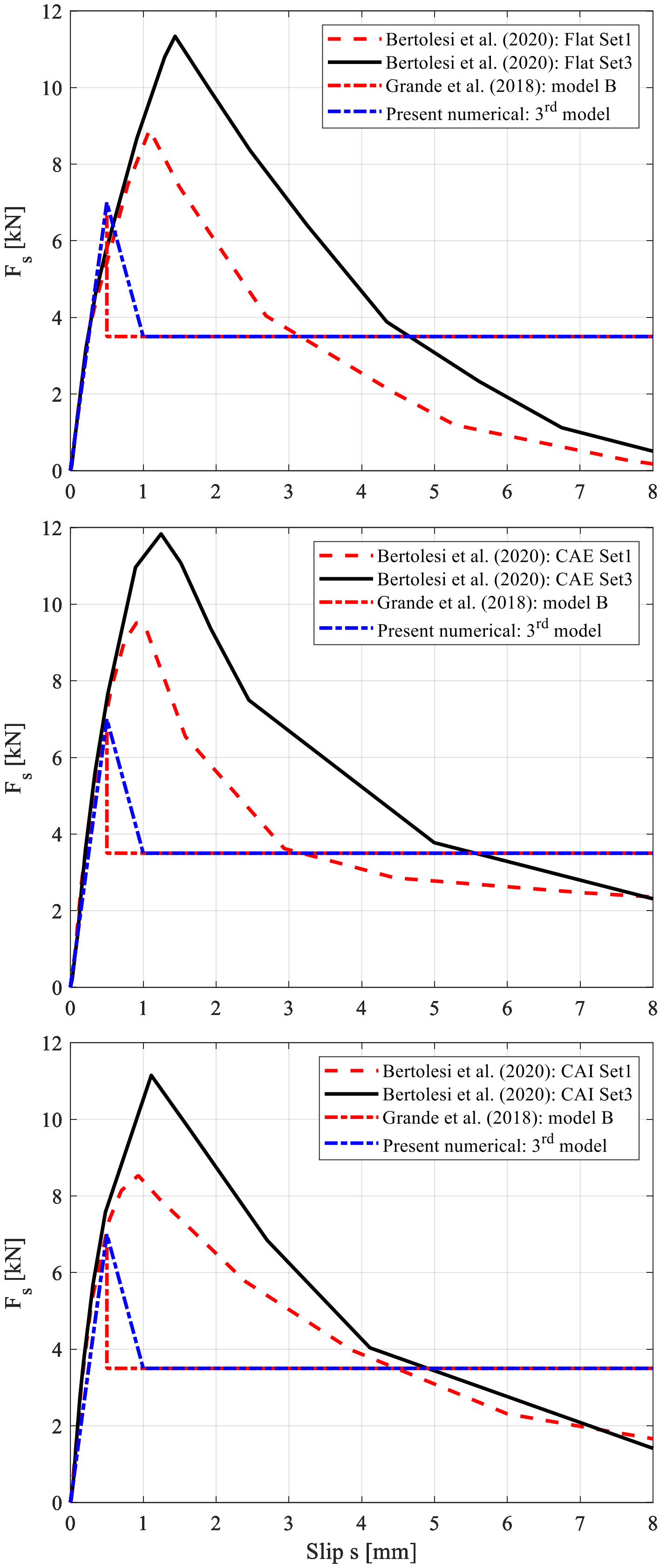

-a

-b

-c

Figure 10: Spike $F_s - s_s$ shear behavior obtained from Abaqus FE post processed results (Set 1 and Set 3 mechanical properties) and hypotheses assumed here and by Grande et al. [48] -a: Flat. -b: CAE. -c: CAI.

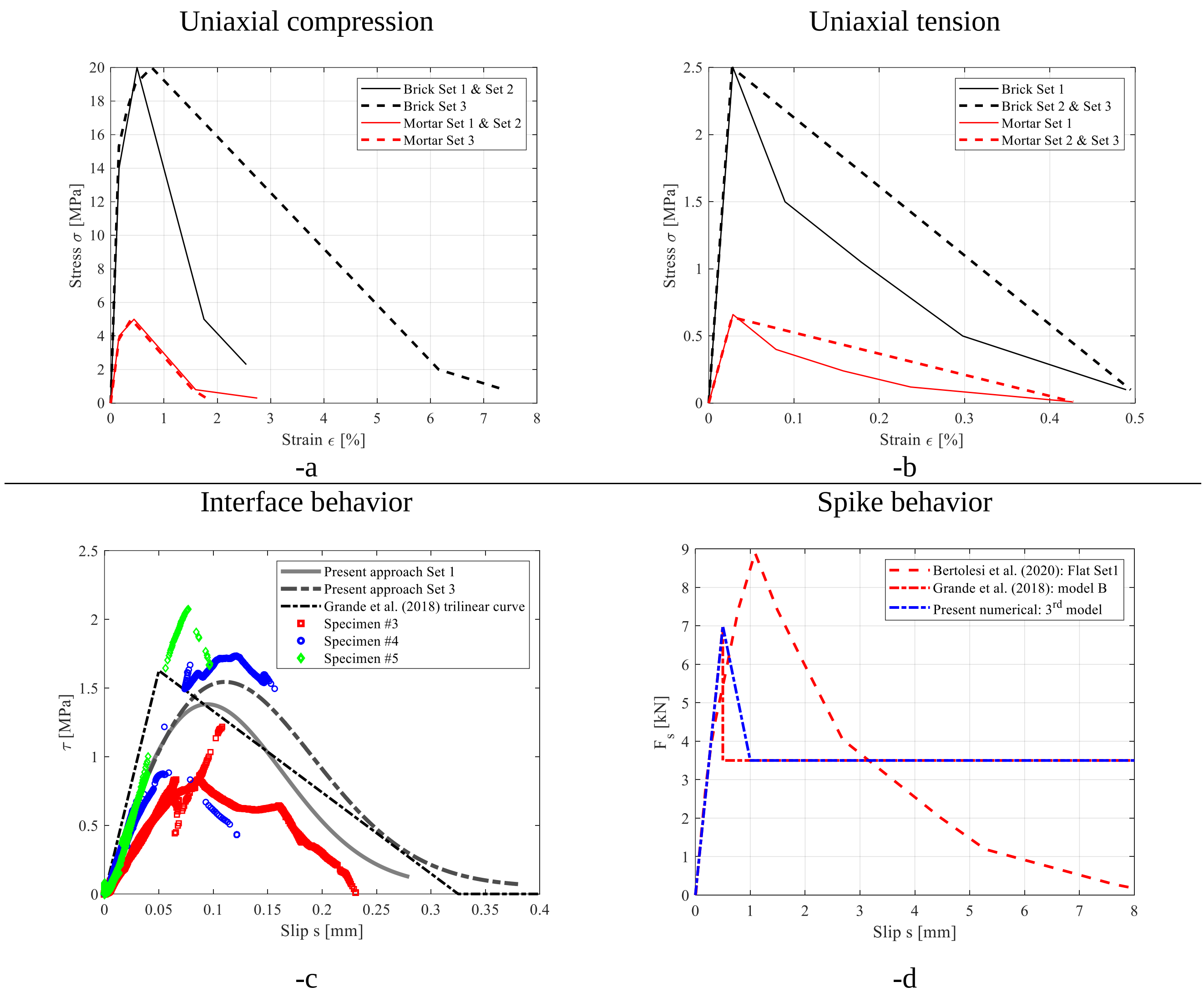

Figure 11:–a & b: assumptions made for bricks and mortar by Bertolesi et al. [52] in the heterogeneous FE approach (-a: compression; -b: tension). -c: interface behavior adopted in the present simulations and comparison with experimental data and previously presented trilinear approach. -d: Spike behavior adopted in the 3rd hypothesis in the present paper and comparison with Set 1 data by Bertolesi et al. [52] and numerical approach by Grande et al. [48].

4. Numerical results

In this Section, the results obtained with the numerical model previously discussed, in presence of anchor spike both for the flat and curved cases, are presented and critically compared with both experimental evidences and the results deduced from recent models developed by the authors to fit experimental data, relying on a FE discretization with springs [48]. In this latter approach, the presence of the spike in [48] is accounted for adding two uncoupled springs, one for the normal and one for shear action, respectively. Figure 10 depicts the spike shear force-slip ($F_s - s_s$) behavior obtained post processing Abaqus FE results from past investigation [52]. The interested reader is referred to [52] for further detail of the model. Results are commented especially in light of their dependence on the mechanical properties assumed for the anchor spike and the interface.

In Figure 12, the global force-displacement curve obtained with the proposed model for the flat case (continuous black curve for Set 1 data and dashed black curve for Set 3) are compared with both experimental data and two previously presented numerical approaches by the authors (one with damage in the bulk [52], the other with non-linear interfaces between substrate and FRP based on a FE discretization with springs [48]).

As it can be observed, the agreement with previously presented numerical approaches is very satisfactory, meaning that both the FRP/substrate interface law and the spike anchor behavior are model suitably grounding on convincing assumptions. It is particular evident the point of activation of the spike, where a sudden change in the load carrying capacity and in its first derivative are observed. Full delamination occurs obviously at different displacements because the interface laws adopted differ for the fracture energies assumed, so that Set 3 is more ductile than Set 1. As expected, the interface behavior is globally very similar to that obtained with damage in the bulk (compare respectively the continuous black curve with the dashed red one and the dashed back curve with the dashed green one, which correspond in pair to Set 1 and Set 3 mechanical properties of [52]). In the Abaqus model proposed in [52], obviously there is not that limit in the ductility which reflect in the global behavior with a sudden drop of the load carrying capacity, because of the fact that damage occurs exclusive in the bulk of the substrate and softening spreads progressively inside the volume, excluding the possibility of sudden drops of the global load carrying capacity. In any case the global results appear in very good agreement with both Abaqus approach by Bertolesi et al. [52] and the interface model by Grande et al. [48].

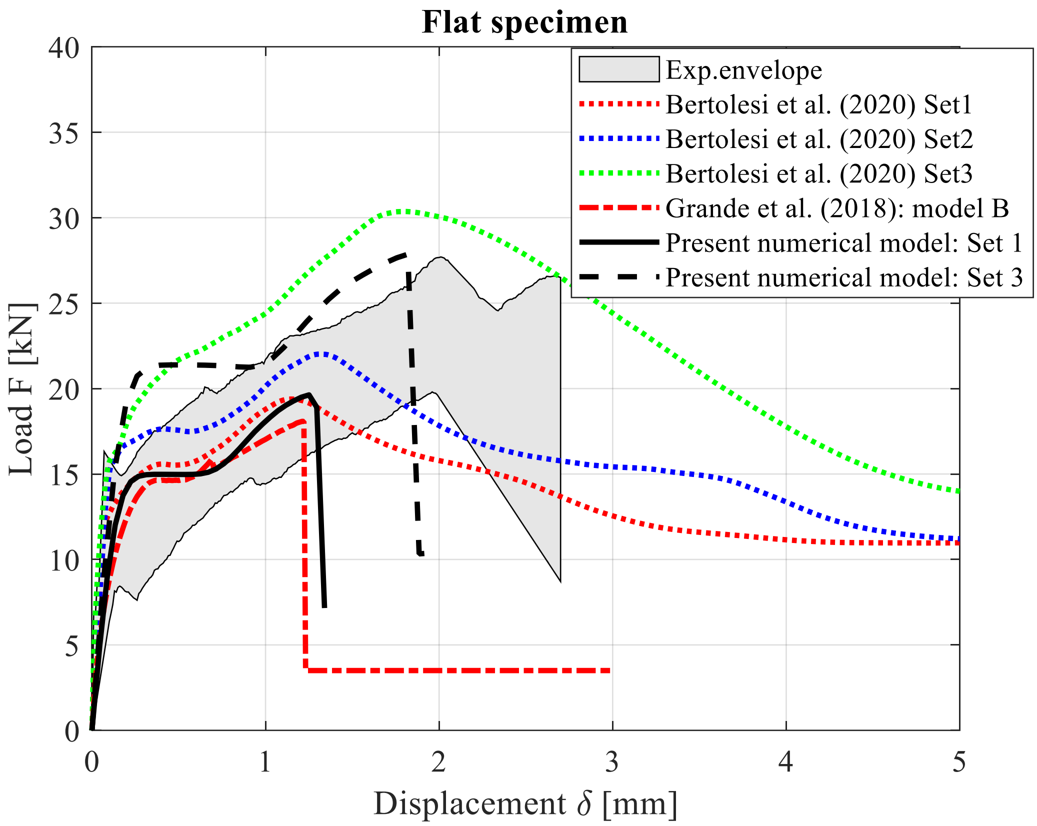

Figure 12: Flat specimen, global load-displacement curves. Comparison among present model, Grande et al. [48] numerical model, Bertolesi et al. [52] numerical model and experimental data.

As far as the evolution of interface slip and the stresses at the interface between FRP and substrate and on FRP are concerned, Figure 13 depicts such results at progressive values of displacement s_0 applied at the loaded edge. In particular, subfigure -a depicts the interface slip function at increases s_0 values, subfigure -b tangential stress at the interface and subfigure -c fiber tensile stress. Left column refers to Set 1 mechanical properties, whereas right column to Set 3 mechanical properties.

First of all, the stability of the algorithm is worth noting, with an evident excellent robustness even for s_0 values corresponding to full debonding, i.e. in that range where global softening is particularly severe. This is certainly an intrinsic advantage of the numerical procedure adopted, especially when compared with a standard FE approach. Second, the role played by the anchor spike is particularly evident, especially as far as the normal stress plot in the FRP strip is concerned (subfigure -c). It is indeed quite noticeable the jump of the normal stresses in correspondence of the spike, which increases in a visible manner only at reasonably large values of the displacement applied at the loaded edge, i.e. near 0.7 and 1 mm for Set 1 and Set 3, as deducible from the global behavior reported in Figure 12.

Figure 14 shows for the flat specimen the numerically obtained force-slip curves on spike: Set 1 results are represented by a continuous black curve, whereas Set 3 by a dashed line. As immediately visible, the spike activates with its maximum load carrying capacity late during the deformation process and failure occurs for the total debonding of the FRP from the substrate rather than for a failure of the spike itself, which exhibits finally a drop in the load carrying capacity because the local slip on the spike is not linearly dependent by the applied displacement s_0 at the loaded edge, a feature which makes the model bypass the potential peak load carried by the spike.

Finally, in Figure 15 a comparison between present numerical predictions and experimental evidence for strain gauges SG01 and SG02 are depicted, as usual representing Set 1 data on the left and Set 3 on the right column. It is worth mentioning that experimental shear stresses on the interval between spike and SG02, deduced from SG02 experimental data, are always linear because it was made the simplistic hypothesis of assuming the spike subjected to a slip equal to zero. This notwithstanding the experimentally deduced information is useful, because it provides a rough estimation of the stiffness of the reinforcing system in correspondence of the interval between SG02 and the spike. Obviously, shear and normal stresses deduced from strain gauges information refer for SG01 to the interval between SG01 and SG02, and for SG02 to the interval between SG02 and the spike. Such procedure is obviously repeated identically for CAI, CAE, CBE and CBI specimens. For the sake of brevity from now ongoing, the Authors will refer directly to strain gauges instead of the aforementioned intervals.

After a careful analysis of the results obtained, it can be affirmed that Set 1 interface behavior reproduces better the elastic phase, whereas Set 3 data seem much more in agreement with experimental evidences in the non-linear range. According to authors opinion such result maybe could be a consequence of the better quality of the specimens assembled in case of the anchor spike, which exhibit also an experimental interface behavior better than that observed for the specimens without anchor spike, compare for instance Figure 6 and Figure 8-b.

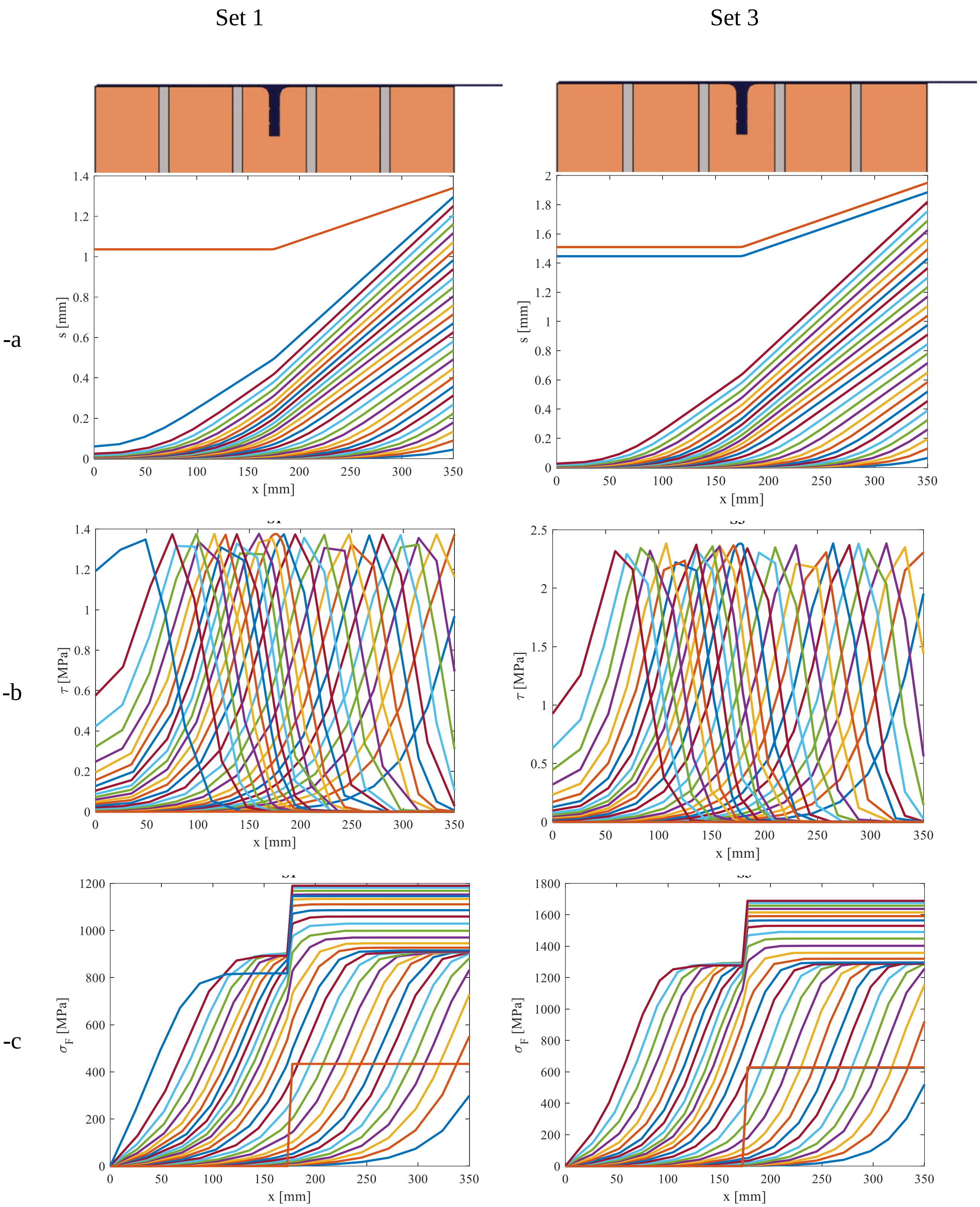

Figure 13: Flat specimen. –a: abscissa x-slip diagram –b: abscissa x- tangential stress at the FRP substrate interface. –c: abscissa x- normal stress in FRP reinforcement. Left column: Set 1 mechanical properties. Right column: Set 3 mechanical properties.

421

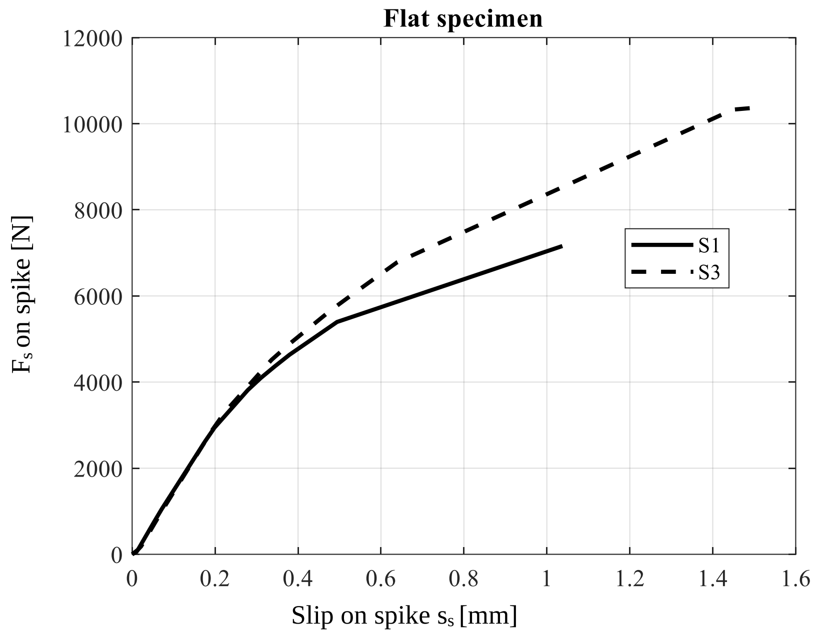

Figure 14: Flat specimen, force-slip curves on spike obtained numerically.

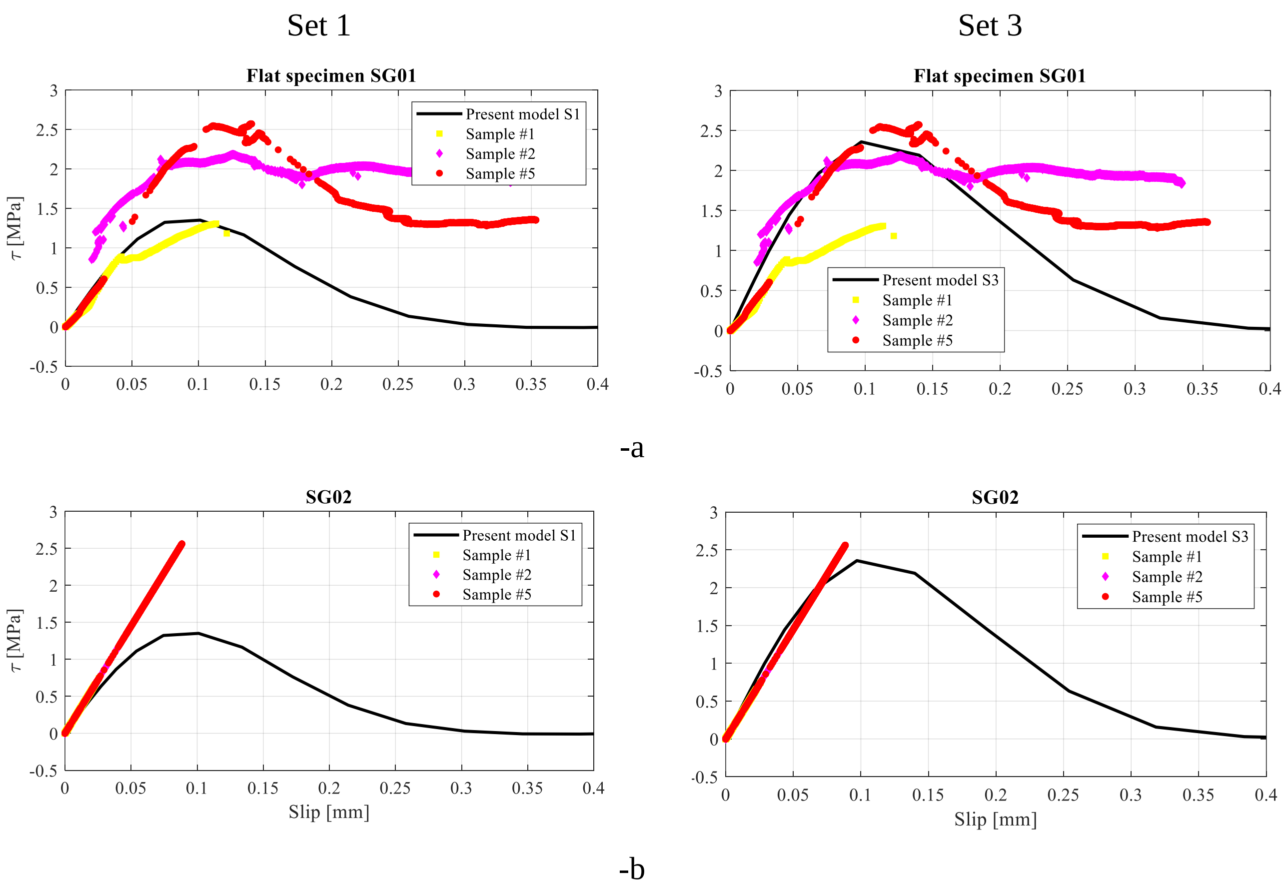

Figure 15: Flat specimen with anchor spike, tangential interface stresses. Comparison between numerical prediction (Set 1 left and Set 3 right) and experimental data provided by strain gauges SG01 (-a) & SG02 (-b).

As far as the specimens with flat configuration are concerned, global force-displacement curves obtained for CAI, CAE, CBI and CBE are shown in Figure 16, again showing experimental data envelopes and previously presented numerical models.

From an overall analysis of the global results obtained, the same considerations done for the flat case can be repeated:

- The activation of the spike occurs late during the test, with a visible increase of the load carrying capacity an in its first derivative.
- Set 1 and Set 3 data assumed in this paper for both the spike and the interface result in curve appearing in very good agreement with those presented by Bertolesi and co-workers in [52]. This is not surprising, because the assumptions made in the present paper are in reasonable agreement with those done in [52], where however a model with damage in the bulk of the substrate was used, without any kind of non linearity at the FRP substrate interface.
- The sudden drop of the load carrying capacity visible in the present model is again a consequence of the full debonding at the interface, which is obviously not visible in a model where damage is diffused in the bulk.
- Set 1 results are also in excellent agreement with Grande et al. model [48], since the only differences between the approaches are two: (i) a slight different behavior of the interface (exponential here and trilinear in [48]) and (ii) a different constitutive model assumed for the spike (here derived from Abaqus post processed results and in [48] assumed elasto-fragile).
- As far as the effect of the curvature is concerned, it may be pointed out how the intrados reinforcement is less effective even in presence of anchor spike, with peak strength and ductility sensibly lower than those found for the specimens reinforced at the extrados, especially at high curvatures. The exploitation of the spike is indeed sensibly lower for CAI if compared to that for CAE, see for instance Figure 17, where the numerically obtained force-slip curves on spike are represented for both sets of material properties assumed in the four different cases of curvatures analyzed. Such results are intuitively in agreement with a Mohr-Coulomb behavior of the interface, which is subjected to tensile normal stresses for CAI and CBI and to beneficial compression for CAE and CBE. Rather noticeable is finally the agreement between present numerical predictions and experimental evidences reported in [46], also considering the unavoidable scatter exhibited by experimental data in presence of a limited number of replicates.

From Figure 18 to Figure 21, interface slip s (subfigures –a), tangential stress τ (subfigures –b), FRP axial stress σ_F (subfigures –c) and interface normal stress σ_n (subfigures –d) at different values of the applied displacement s_0 at the loaded edge are depicted. Figures refer in order respectively to CAE (Figure 18), CBE (Figure 19), CAI (Figure 20) and CBI (Figure 21). The same considerations done for the flat case can be repeated here, with an evident role played by the spike in increasing locally the load carrying capacity at relatively large displacements applied at loaded edge.

It is also interesting to notice how the curvature plays a beneficial role when the reinforcement is applied at the extrados, because compression stresses arise at the FRP/support interface, especially for CAE, with an observed peak normal stress exceeding 0.17 and 0.24 MPa at the loaded edge immediately before delamination for Set 1 and Set 3 respectively, see Figure 18-d.

The opposite behavior is observed for the reinforcement glued at the intrados, especially for a large curvature of the interface (CAI), where a positive normal stress of about 0.12 and 0.18 MPa is present immediately before debonding for Set 1 and Set 3 respectively, see Figure 20-d. Since the interface obeys as a Mohr-Coulomb failure criterion, both the load carrying capacity and the ductility of the strengthened curved pillar become larger with reinforcement at the extrados, where the interface compression normal stress plays a beneficial role.

The comparison between the numerical prediction deduced by accounting for Set 1 and Set 3 mechanical properties and experimental data provided by strain gauges is shown in Figure 22 to Figure 25 for the specimens with anchor spike. The plots generally show, in the majority of cases, a good agreement between numerical and experimental results, consistent with the outcomes of the specimens without anchor spikes.

Finally in Figure 26, assuming for the spike the simplified tri-linear relationship shown in Figure 11-d and labeled as "3rd present numerical model", the global load-displacement curves obtained for the flat case, CAE, CAI, CBE and CBI are depicted and compared with both experimental envelops and numerical predictions by Grande et al. [48],. Not surprisingly, the results are almost superimposable to those found in [48], because both the interface model and the spike shear force-displacement relationship adopted in two approaches are very similar.

As can be observed in Figure 10, the constitutive model assumed in this latter case for the spike is quite different from that deduced by Abaqus computations and there is no variability with the curvature of the specimen, as it should be. This notwithstanding, the results appear fully in agreement with the experimental data, simply because the activation of the strength of the spike depends on the local slip of the anchorage in the different cases and the peak strength of the device is never reached, as clearly visible by Figure 17 in the case of the four curved surfaces investigated.

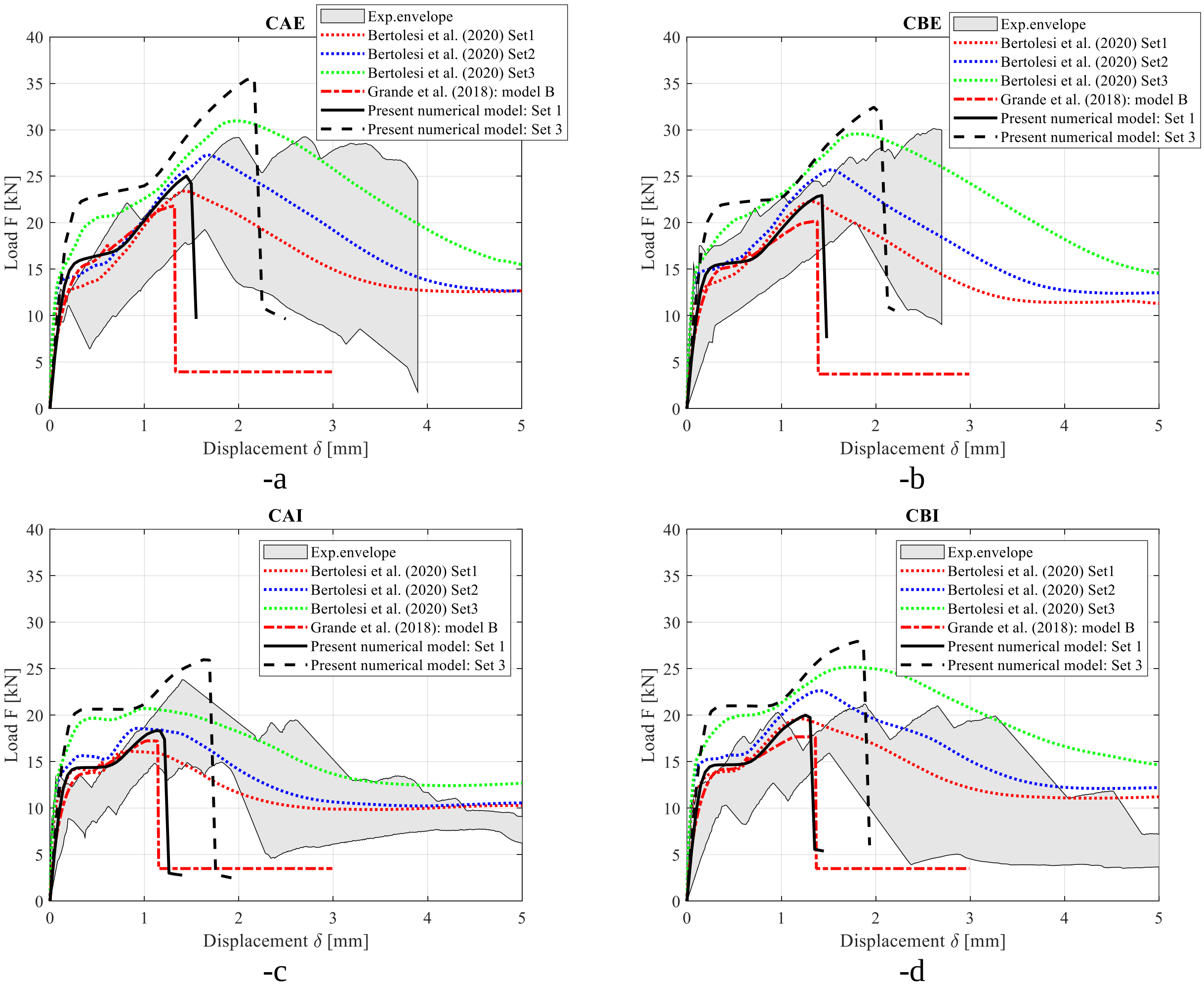

Figure 16: Global load-displacement curves obtained with the present approach (continuous black curve: Set 1; dashed black curve: Set 3). Comparison among present model results, experimental evidences and previously presented models.–a: CAE. –b: CBE. –c: CAI. –d: CBI.

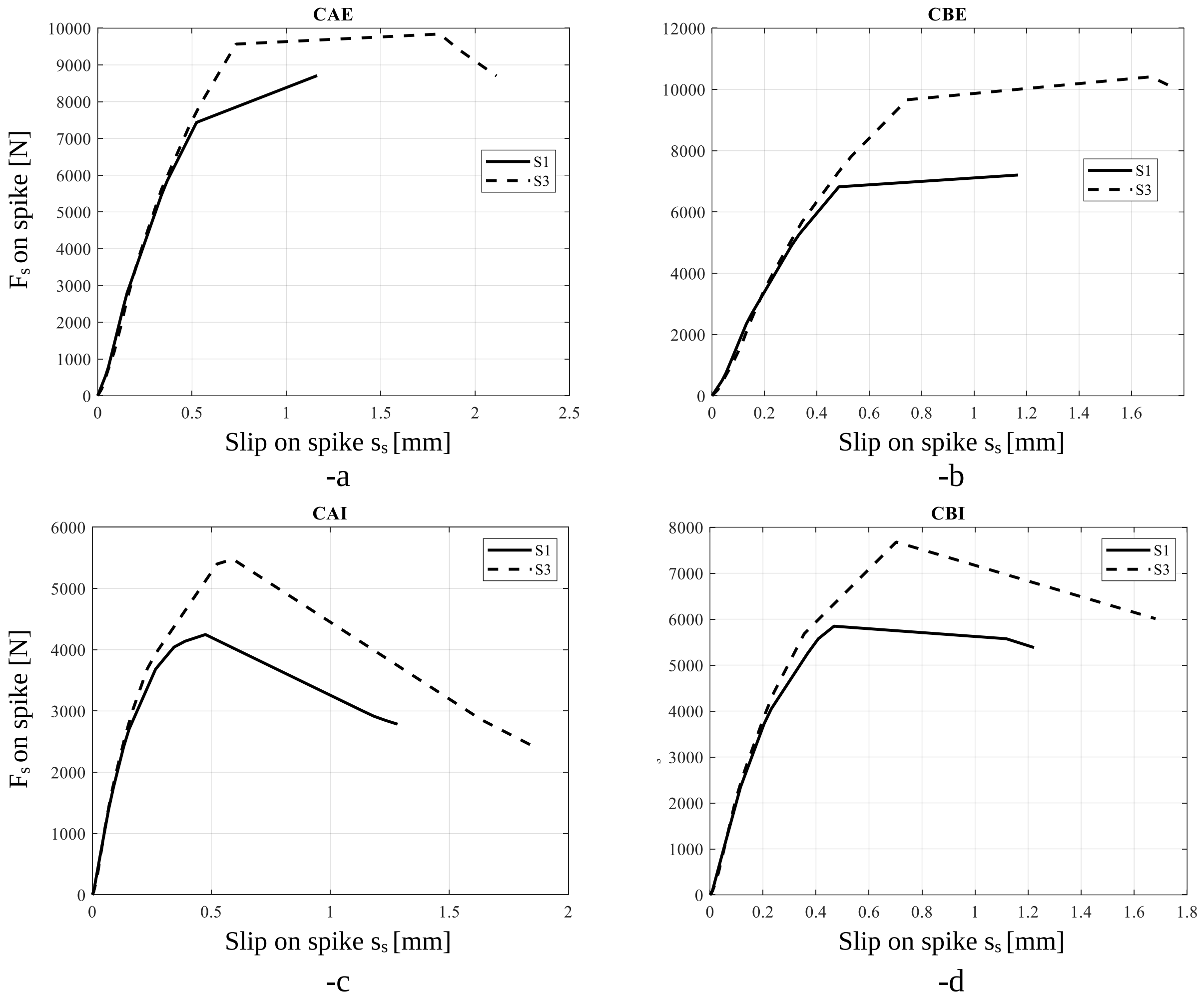

Figure 17: Spike slip-shear force behavior in the numerical model proposed (continuous black curve: Set 1; dashed black curve: Set 3).–a: CAE. –b: CBE. –c: CAI. –d: CBI.

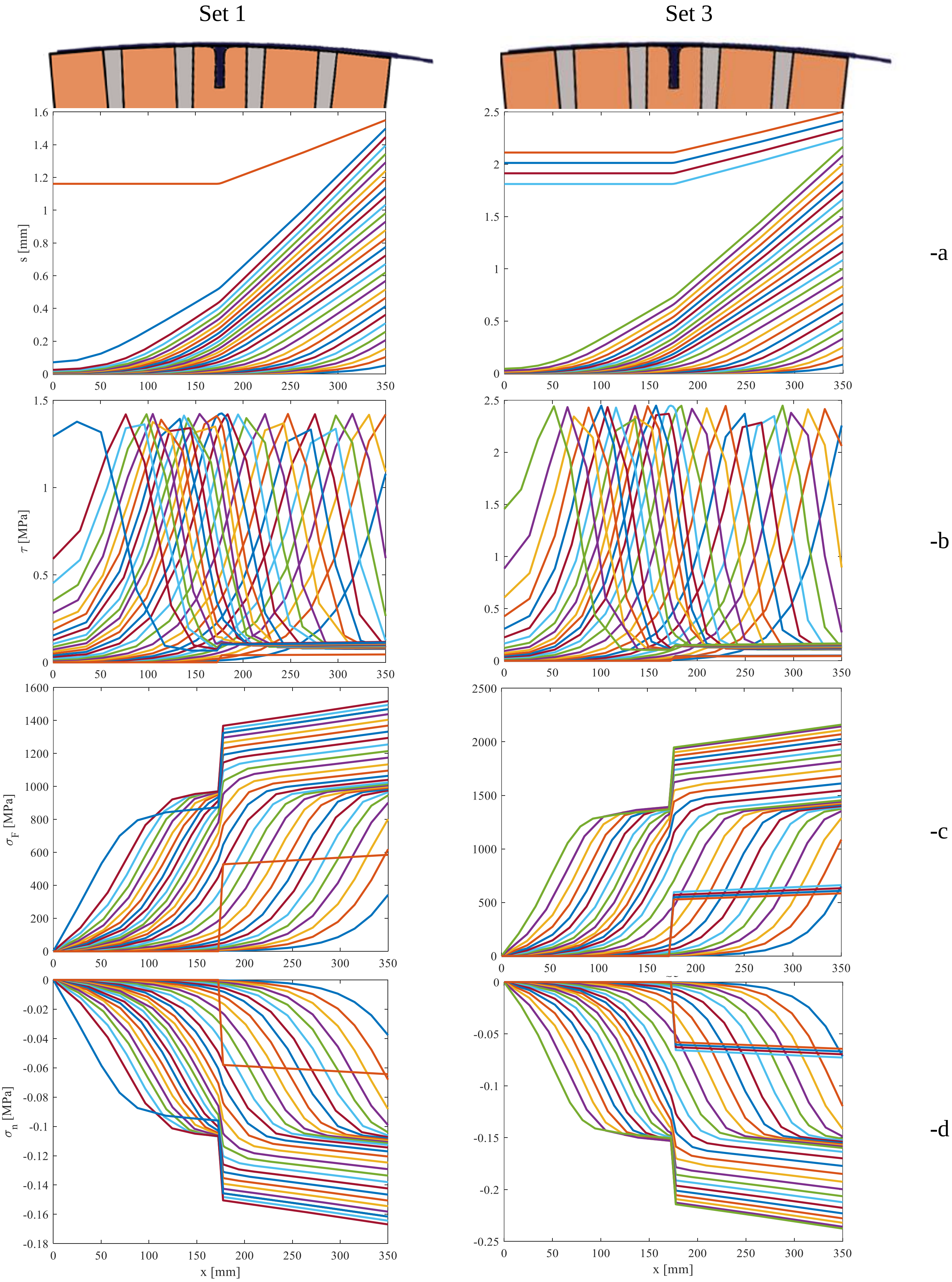

Figure 18: CAE with anchor spike, –a: x-slip diagram –b: x- tangential stress at the FRP substrate interface. –c: x- normal stress on FRP. –d: x- stress normal to the FRP/substrate interface.

494

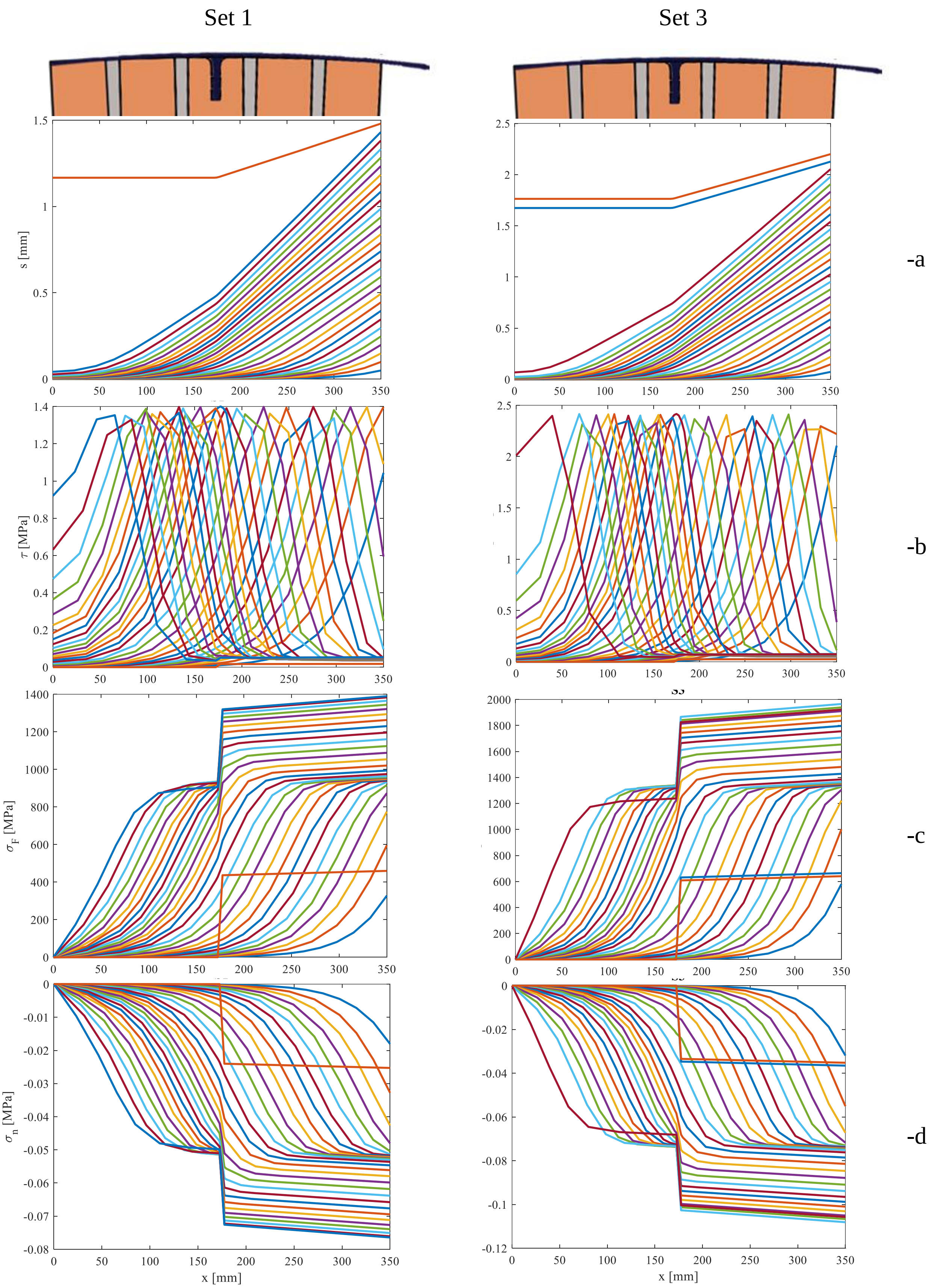

Figure 19: CBE with anchor spike, –a: x-slip diagram –b: x- tangential stress at the FRP substrate interface. –c: x- normal stress on FRP. –d: x- stress normal to the FRP/substrate interface.

495

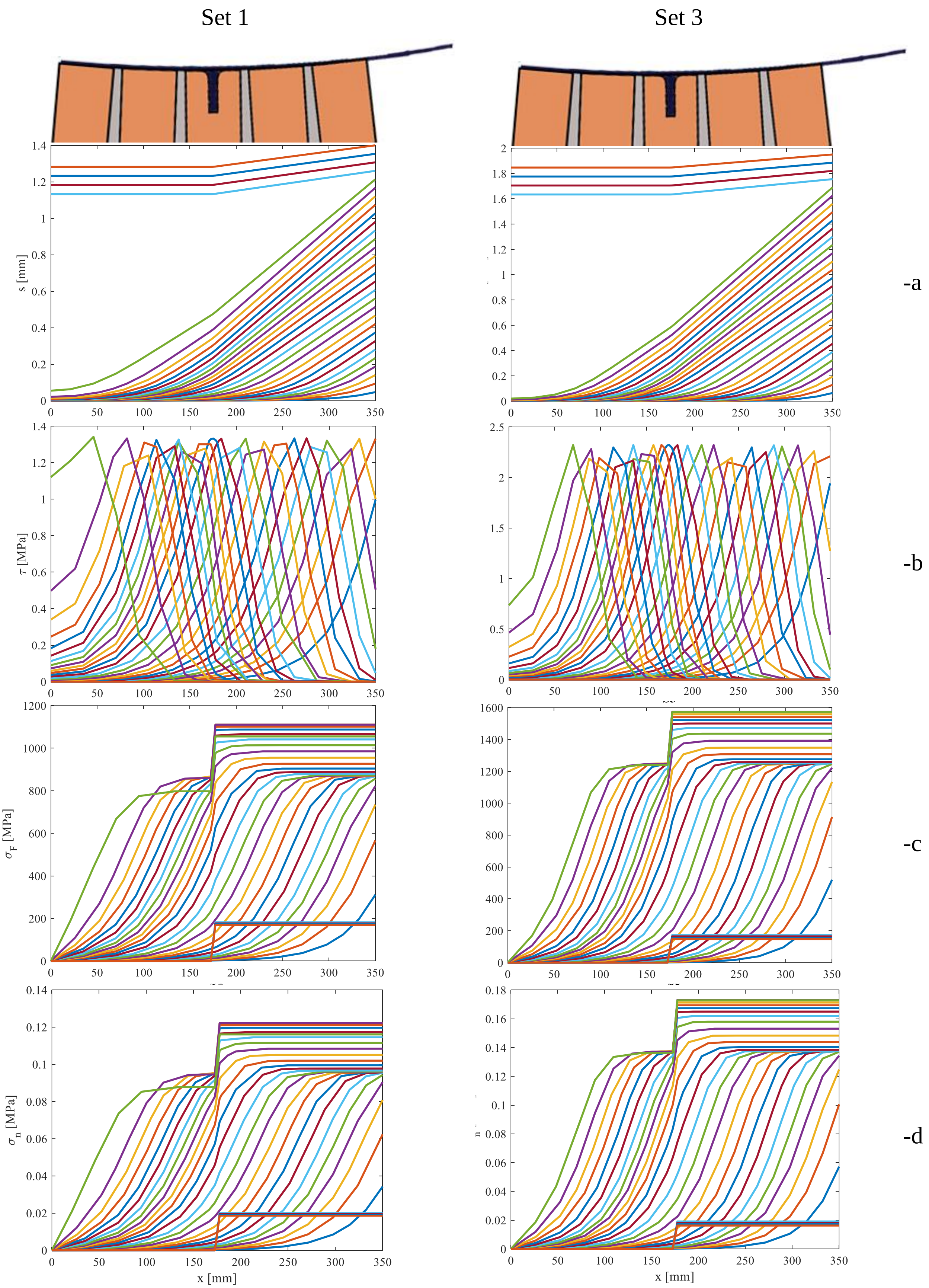

Figure 20: CAI with anchor spike, –a: x-slip diagram –b: x- tangential stress at the FRP substrate interface. –c: x- normal stress on FRP. –d: x- stress normal to the FRP/substrate interface.

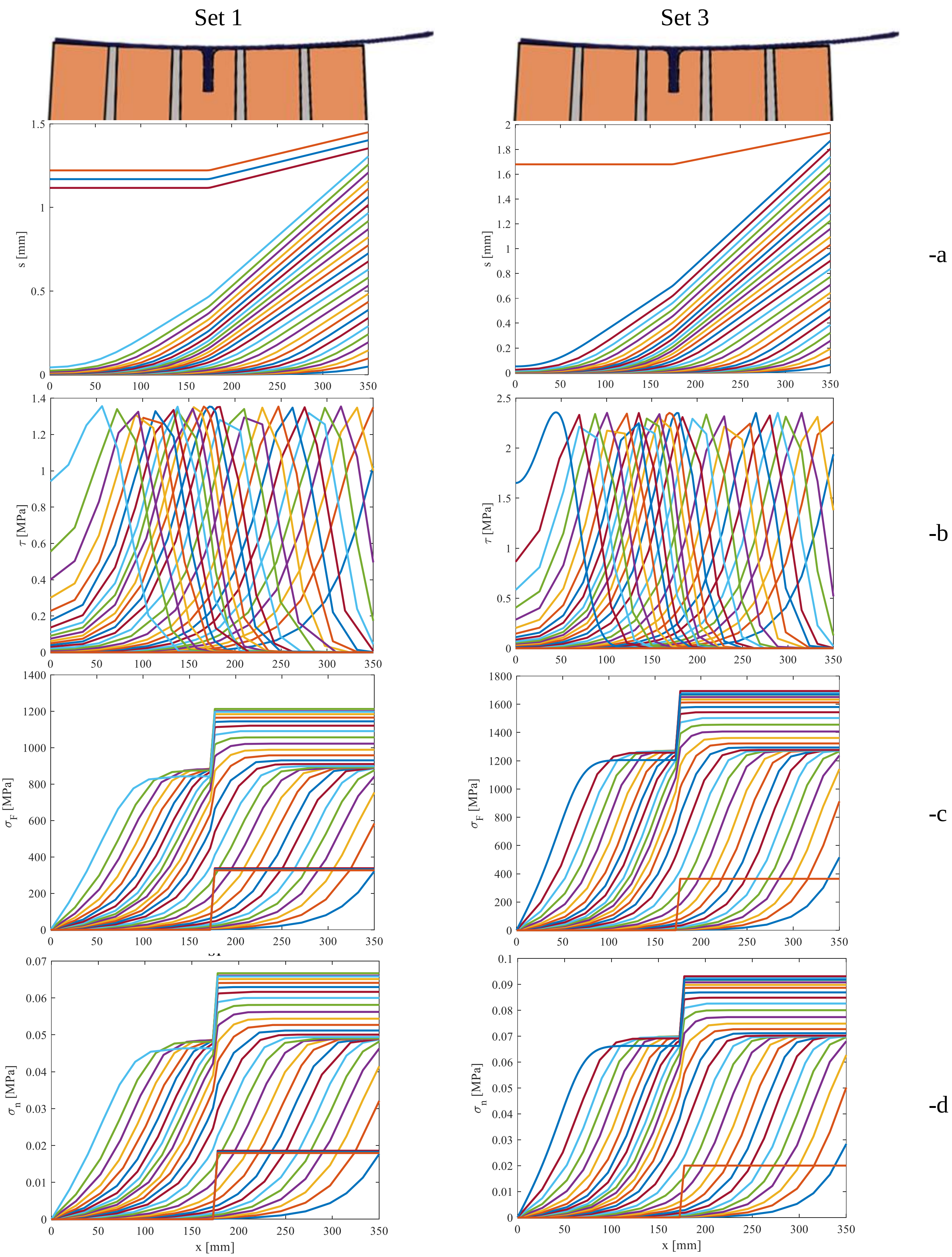

Figure 21: CBI with anchor spike, –a: x-slip diagram –b: x- tangential stress at the FRP substrate interface. –c: x- normal stress on FRP. –d: x- stress normal to the FRP/substrate interface.

Set 1 Set 3

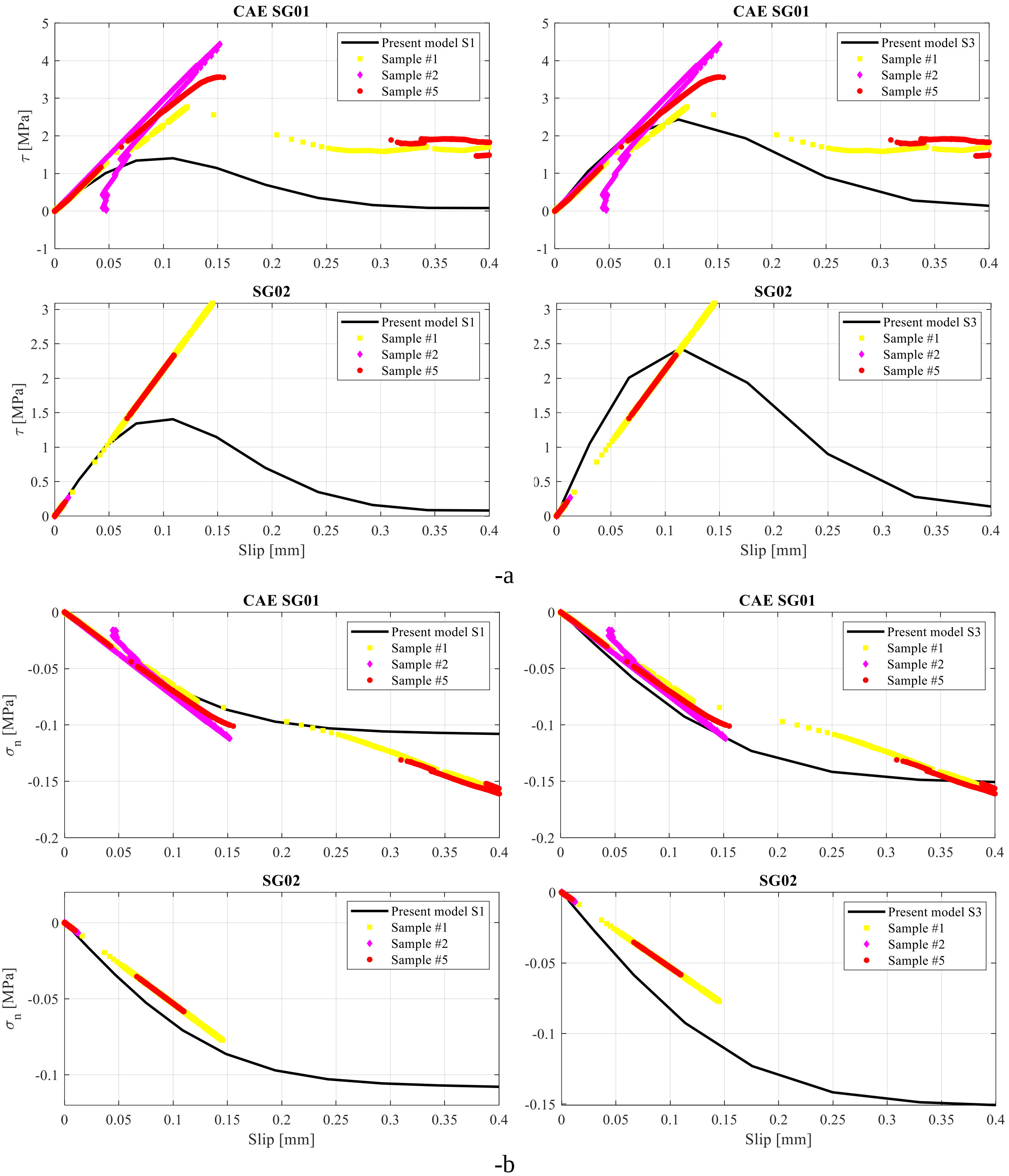

Figure 22: CAE specimen with anchor spike, tangential (-a) and normal (-b) interface stresses. Comparison between numerical prediction and experimental data provided by strain gauges SG01 & SG02. Left column: Set 1 mechanical properties. Right color: Set 3 mechanical properties.

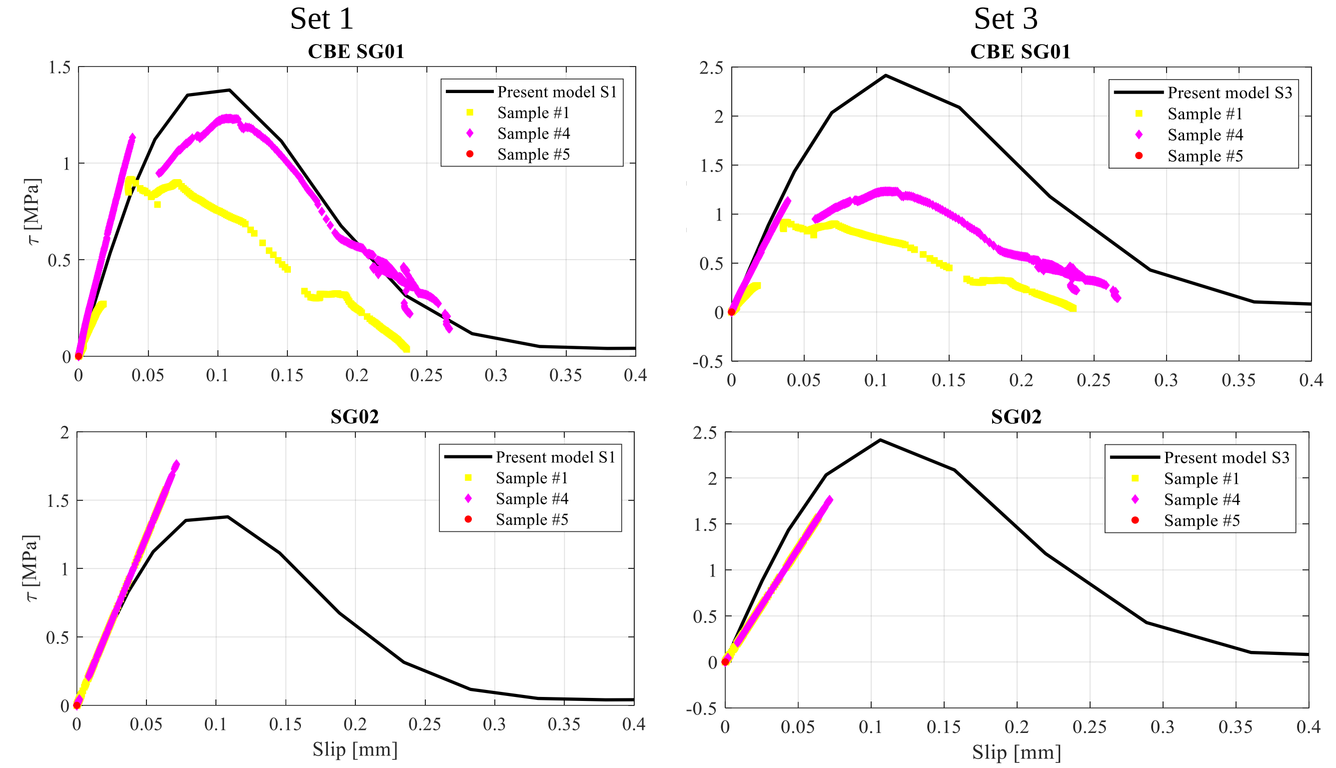

-a

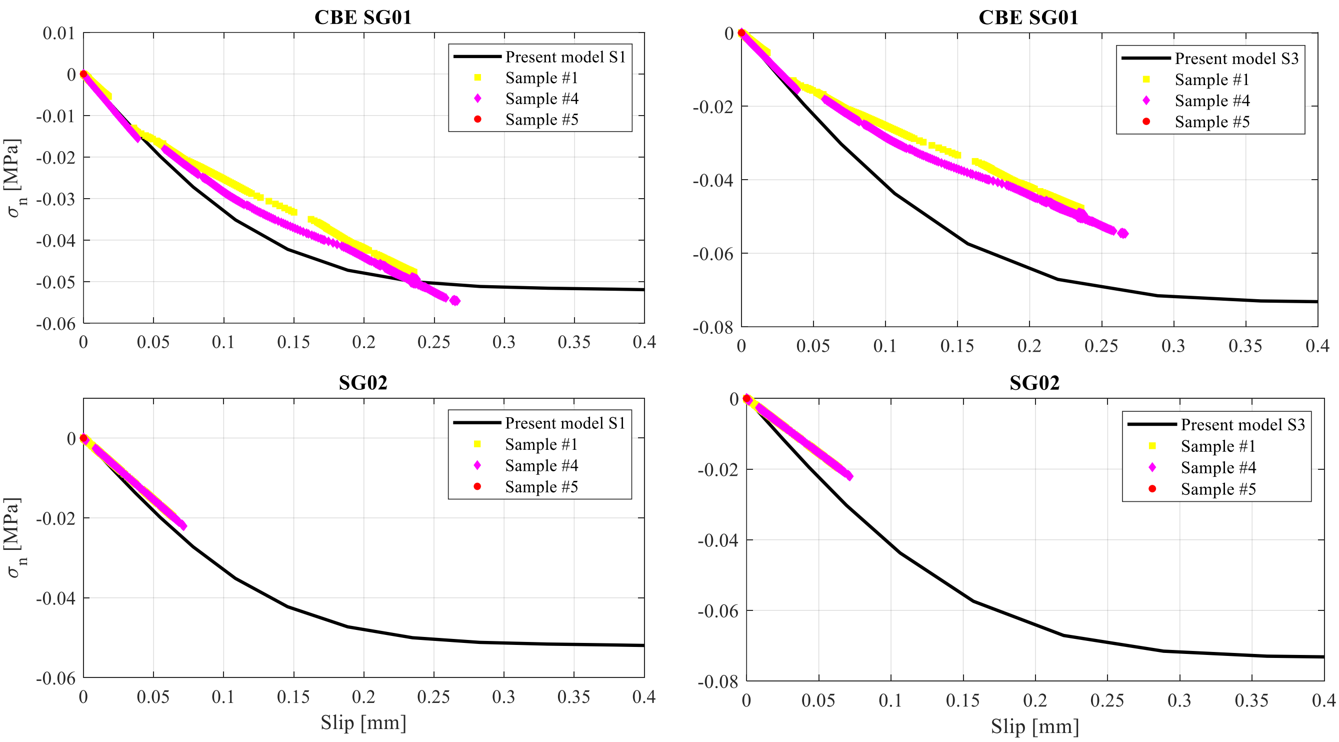

-b

Figure 23: CBE specimen with anchor spike, tangential (-a) and normal (-b) interface stresses. Comparison between numerical prediction and experimental data provided by strain gauges SG01 & SG02. Left column: Set 1 mechanical properties. Right color: Set 3 mechanical properties.

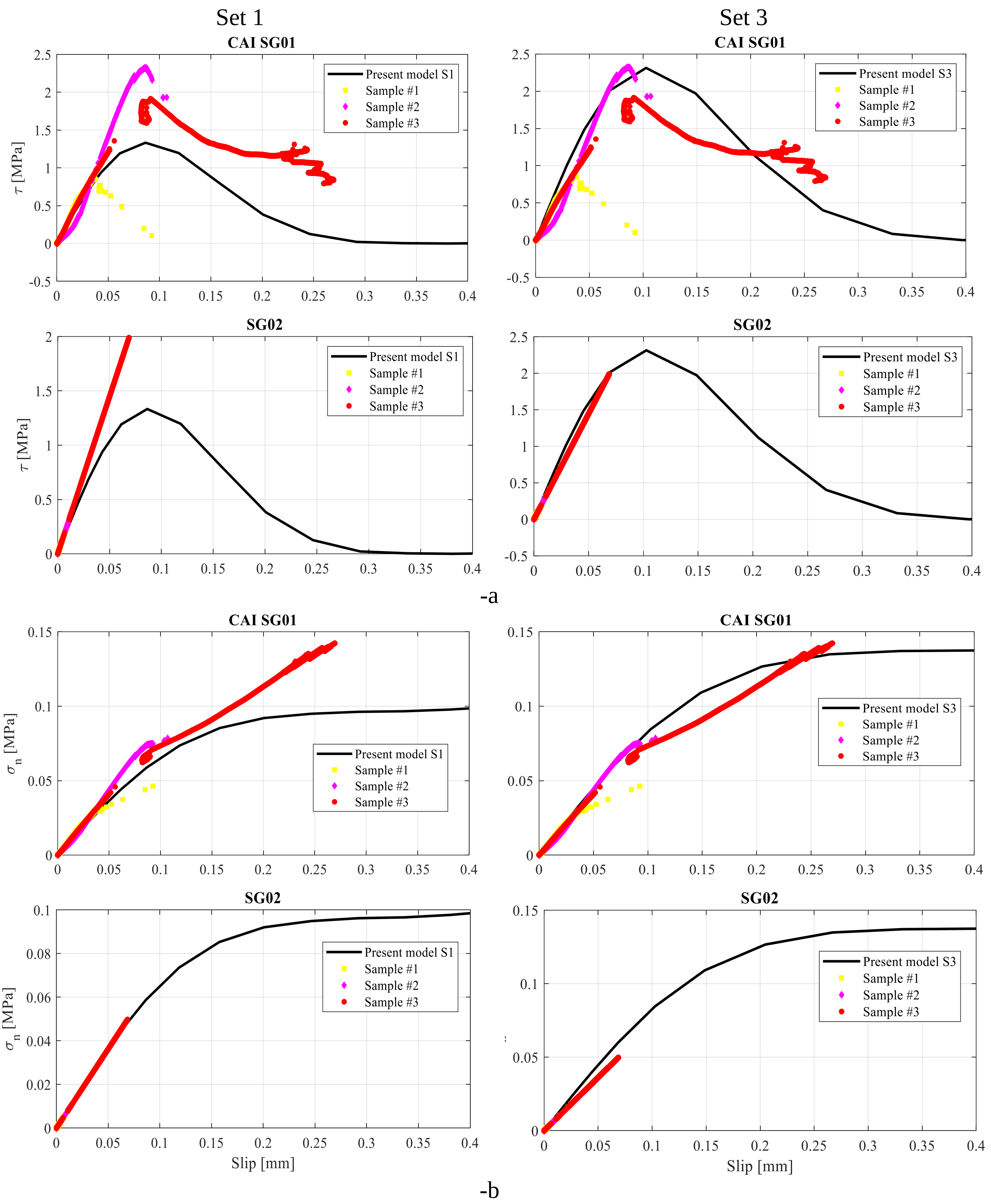

Figure 24: CAI specimen with anchor spike, tangential (-a) and normal (-b) interface stresses. Comparison between numerical prediction and experimental data provided by strain gauges SG01 & SG02. Left column: Set 1 mechanical properties. Right color: Set 3 mechanical properties.

501

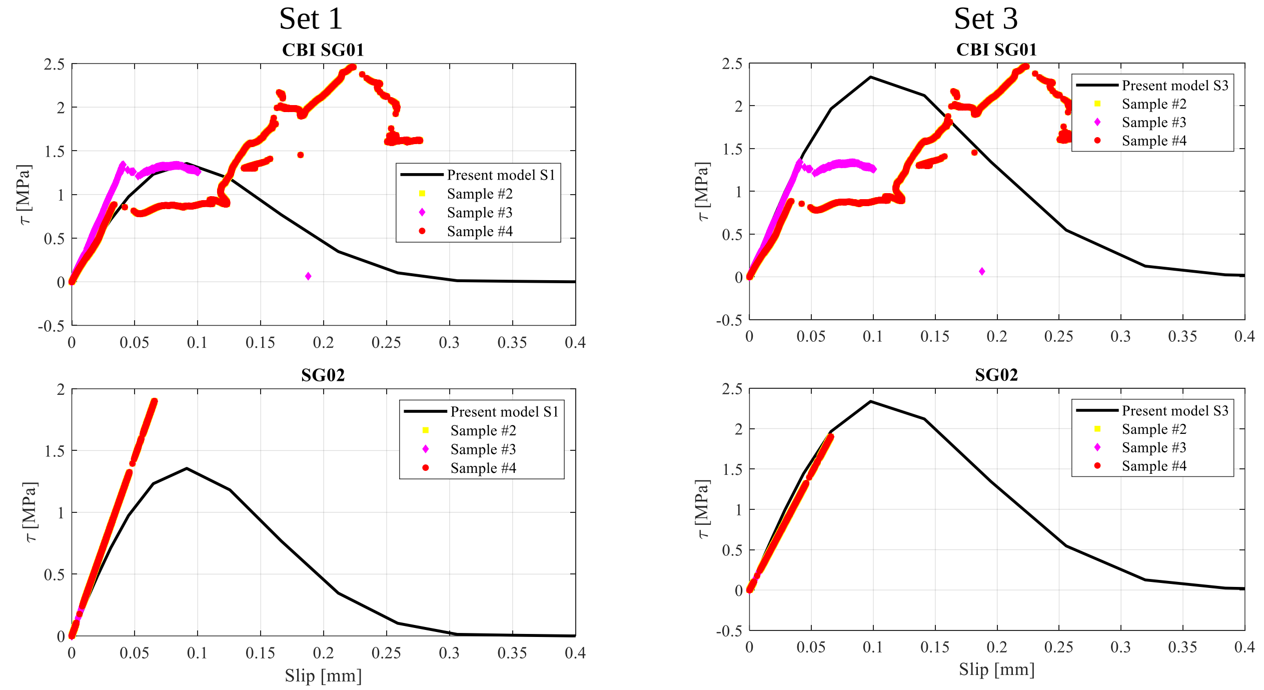

-a

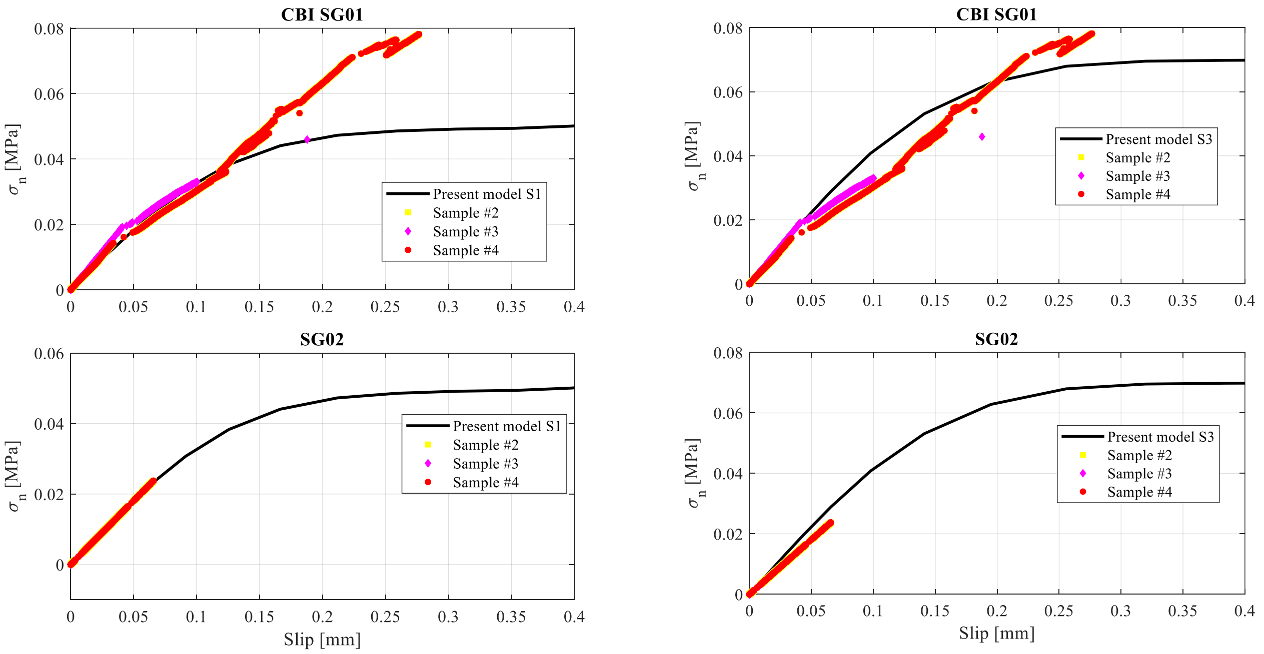

-b

Figure 25: CBI specimen with anchor spike, tangential (-a) and normal (-b) interface stresses. Comparison between numerical prediction and experimental data provided by strain gauges SG01 & SG02. Left column: Set 1 mechanical properties. Right color: Set 3 mechanical properties.

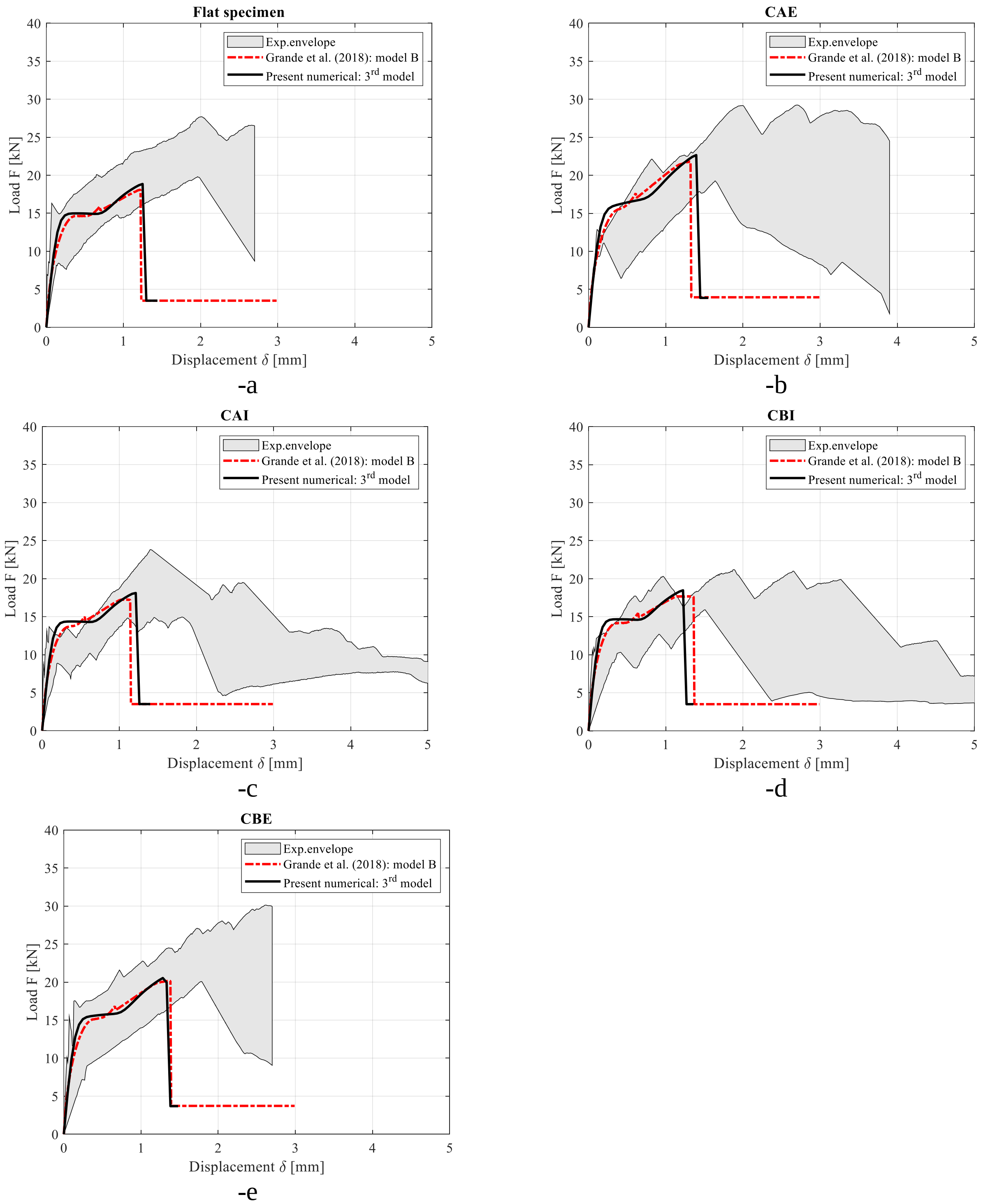

Figure 26: Global load-displacement curves obtained with the present approach assuming the spike relationship reported in Figure 11-d. Comparison among present model results, experimental evidences and previously presented model by Grande et al. [48]–a: Flat. –b: CAE. –c: CAI. –d: CBI. -e: CBE.

5. Conclusions

Structural rehabilitation of masonry constructions throughout FRPs generally involves elements with a curved configuration, such as arches, vaults, domes, etc. In these cases, the bond behavior of the reinforcing system, and consequently its performance, is particularly influenced by the curvature geometry and the position of the reinforcement (i.e. at the extrados or intrados). Moreover, in order to prevent premature failures due to tensile stresses normal to the direction of reinforcement, arising in case of applications at the intrados, mechanical anchors are nowadays generally employed in current practice. The presence of this additional component further influences the bond behavior of FRPs applied on curved masonry substrates. Indeed, a recent and current field of research just concerns the study of the bond behavior of FRP applied to curved masonry structures throughout both experimental tests and numerical modeling strategies.

In this context, the present paper has presented an interface exponential model for simulating the bond behavior of curved masonry pillars reinforced with FRP strips applied to the masonry substrate by both epoxy adhesive and anchor spikes. The proposed model has been based on a relatively simple BVP obtained by assuming for the spike a constitutive behavior under shear forces quantitatively deduced from post processing of numerical data obtained by a FE micro-modelling approach. After a detailed discussion reported in the first part of the paper, the reliability of proposed model has been assessed with reference to experimental cases object of a previous research carried out by the authors.

The obtained results have shown the reliability of the proposed model in reproducing the experimental results both concerning global response, analyzed in the paper in terms of force-displacement curves and, also, local behavior in terms of shear stress and normal stress vs. slip curves. The stability of the solution of the BVP has been clearly shown together with the capacity of the proposed model to capture the main phases of the bond behavior prior and after the activation of the spike anchor.

In the paper it has been also reported the comparison with the results obtained by the authors throughout other modeling approaches based on both a detailed and simplified finite element approach, object of previous studies. The outcomes emerged from this additional comparison have underlined features useful for further assessing the hypotheses at the basis of the proposed model particularly in terms of constitutive laws of both masonry and reinforcement-masonry interface. In particular, it has been possible to quantitatively deduce a constitutive behavior of the spike anchor under shear forces from a post processing of numerical data obtained by a previous research of the authors, where the debonding process was modelled in ABAQUS FEM software assuming damage propagating in the bulk substrate.

In conclusion, the proposed approach:

- allows to skip the high computational burden required to capture the behaviour of anchored FRP reinforcement.
- simplifies the geometric problem of the spike anchoring and the related dimensional inaccuracies or mesh refinement problems that can arise using traditional FEM strategies.
- provides stable solutions during the whole debonding process and accurate results both locally (tangential stress distributions) and globally (force-displacement responses).
- requires a quick calibration involving few mechanical parameters.
- is extendable to different spike anchor configurations, provided that the anchoring force is properly calibrated.

- might help practitioners in a preliminary design phase of the strengthening system by underlining the activation of spikes.

6. References

[1] Hamed E, Rabinovitch O. Failure characteristics of FRP-strengthened masonry walls under out-of-plane loads. Eng Struct 2010. https://doi.org/10.1016/j.engstruct.2010.03.016.

[2] Formisano A, Marzo A. Simplified and refined methods for seismic vulnerability assessment and retrofitting of an Italian cultural heritage masonry building. Comput Struct 2017. https://doi.org/10.1016/j.compstruc.2016.07.005.

[3] Witzany J, Brožovský J, Čejka T, Kroftová K, Kubát J, Makovička D, et al. The application of carbon composites in the rehabilitation of historic baroque vaults. Polymers (Basel) 2015. https://doi.org/10.3390/polym7121540.

[4] Carrara P, Ferretti D, Freddi F. Debonding behavior of ancient masonry elements strengthened with CFRP sheets. Compos Part B Eng 2013;45:800–10. https://doi.org/10.1016/j.compositesb.2012.04.029.

[5] Fagone M, Ranocchiai G. Experimental investigation on out-of-plane behavior of masonry panels strengthened with CFRP sheets. Compos Part B Eng 2018. https://doi.org/10.1016/j.compositesb.2018.05.031.

[6] Foraboschi P. Effectiveness of novel methods to increase the FRP-masonry bond capacity. Compos Part B Eng 2016. https://doi.org/10.1016/j.compositesb.2016.09.060.

[7] Grande E, Milani G, Sacco E. Modelling and analysis of FRP-strengthened masonry panels. Eng Struct 2008;30:1842–60.

[8] Grande E, Imbimbo M, Sacco E. Investigation on the bond behavior of clay bricks reinforced with SRP and SRG strengthening systems. Mater Struct Constr 2015;48:3755–70. https://doi.org/10.1617/s11527-014-0437-x.

[9] Capozucca R, Ricci V. Bond of GFRP strips on modern and historic brickwork masonry. Compos Struct 2016;140:540–55. https://doi.org/10.1016/j.compstruct.2015.12.047.

[10] Fedele R, Milani G. A numerical insight into the response of masonry reinforced by FRP strips. The case of perfect adhesion. Compos Struct 2010. https://doi.org/10.1016/j.compstruct.2010.03.014.

[11] Fedele R, Milani G. Assessment of bonding stresses between FRP sheets and masonry pillars during delamination tests. Compos Part B Eng 2012;43:1999–2011. https://doi.org/10.1016/j.compositesb.2012.01.080.

[12] Fedele R, Milani G. Three-dimensional effects induced by FRP-from-masonry delamination. Compos Struct 2011;93:1819–31. https://doi.org/10.1016/j.compstruct.2011.01.022.

[13] Grande E, Imbimbo M, Sacco E. Bond behaviour of CFRP laminates glued on clay bricks: Experimental and numerical study. Compos Part B Eng 2011;42:330–40. https://doi.org/10.1016/j.compositesb.2010.09.020.

[14] Grande E, Imbimbo M, Sacco E. Simple Model for Bond Behavior of Masonry Elements Strengthened with FRP. J Compos Constr 2010;15:354–63. https://doi.org/10.1061/(asce)cc.1943-5614.0000170.

[15] Grande E, Imbimbo M. A simple 1D-Finite Element approach for the study of the bond behavior of masonry elements strengthened by FRP. Compos Part B Eng 2016;91:548–58. https://doi.org/10.1016/j.compositesb.2016.02.005.

[16] Hosseini A, Mostofinejad D, Emami M. Influence of bonding technique on bond behavior of CFRP-to-clay brick masonry joints: Experimental study using particle image velocimetry (PIV). Int J Adhes Adhes 2015. https://doi.org/10.1016/j.ijadhadh.2015.01.015.

[17] Oliveira D V., Basilio I, Loureņo PB. Experimental bond behavior of FRP sheets glued on brick masonry. J Compos Constr 2011. https://doi.org/10.1061/(ASCE)CC.1943-5614.0000147.

[18] Rotunno T, Rovero L, Tonietti U, Bati SB. Experimental study of bond behavior of CFRP-to-brick joints. J Compos Constr 2015;19. https://doi.org/10.1061/(ASCE)CC.1943-5614.0000528.

[19] Valluzzi MR, Oliveira D V., Caratelli A, Castori G, Corradi M, De Felice G, et al. Round Robin Test for composite-to-brick shear bond characterization. Mater Struct Constr 2012;45:1761–91. https://doi.org/10.1617/s11527-012-9883-5.

[20] Ghiassi B, Verstrynge E, Lourenço PB, Oliveira D V. Characterization of debonding in FRP-strengthened masonry using the acoustic emission technique. Eng Struct 2014;66:24–34. https://doi.org/10.1016/j.engstruct.2014.01.050.

[21] Ghiassi B, Marcari G, Oliveira D V., Lourenço PB. Numerical analysis of bond behavior between masonry bricks and composite materials. Eng Struct 2012. https://doi.org/10.1016/j.engstruct.2012.05.022.

[22] Ghiassi B, Xavier J, Oliveira D V., Lourenço PB. Application of digital image correlation in investigating the bond between FRP and masonry. Compos Struct 2013;106:340–9. https://doi.org/10.1016/j.compstruct.2013.06.024.

[23] Fagone M, Ranocchiai G, Briccoli Bati S. An experimental analysis about the effects of mortar joints on the efficiency of anchored CFRP-to-masonry reinforcements. Compos Part B Eng 2015;76:133–48. https://doi.org/10.1016/j.compositesb.2015.01.050.

[24] Briccoli Bati S, Fagone M, Ranocchiai G. The Effects of Mortar Joints on the Efficiency of Anchored CFRP Sheets Reinforcements of Brick-Masonry. Key Eng Mater 2014;624:575–83. https://doi.org/10.4028/www.scientific.net/kem.624.575.

[25] Milani G, Milani E, Tralli A. Upper Bound limit analysis model for FRP-reinforced masonry curved structures. Part I: Unreinforced masonry failure surfaces. Comput Struct 2009;87:1516–33. https://doi.org/https://doi.org/10.1016/j.compstruc.2009.07.007.

[26] Milani G, Milani E, Tralli A. Upper bound limit analysis model for FRP-reinforced masonry curved structures. Part II: Structural analyses. Comput Struct 2009. https://doi.org/10.1016/j.compstruc.2009.07.010.

[27] Mazzucco G, Salomoni VA, Majorana CE. Three-dimensional contact-damage coupled modelling of FRP reinforcements – simulation of delamination and long-term processes. Comput Struct 2012;110–111:15–31. https://doi.org/https://doi.org/10.1016/j.compstruc.2012.06.001.

[28] Bruggi M, Milani G, Taliercio A. Simple topology optimization strategy for the FRP reinforcement of masonry walls in two-way bending. Comput Struct 2014;138:86–101. https://doi.org/https://doi.org/10.1016/j.compstruc.2014.02.012.

[29] Baratta A, Corbi O. Closed-form solutions for FRP strengthening of masonry vaults. Comput Struct 2015;147:244–9. https://doi.org/https://doi.org/10.1016/j.compstruc.2014.09.007.

[30] Elmalich D, Rabinovitch O. Masonry and monolithic circular arches strengthened with composite materials – A finite element model. Comput Struct 2009;87:521–33. https://doi.org/https://doi.org/10.1016/j.compstruc.2009.02.004.

[31] CNR – Advisory Committee on Technical Recommendations for Construction. Guide for the Design and Construction of Externally Bonded FRP Systems for Strengthening Existing Structures. Italy: 2013.

[32] Chiozzi A, Milani G, Tralli A. Fast kinematic limit analysis of FRP-reinforced masonry vaults. I: General genetic algorithm-NURBS-based formulation. J Eng Mech 2017. https://doi.org/10.1061/(ASCE)EM.1943-7889.0001267.

[33] Pintucchi B, Zani N. A simple model for performing nonlinear static and dynamic analyses of unreinforced and FRP-strengthened masonry arches. Eur J Mech A/Solids 2016. https://doi.org/10.1016/j.euromechsol.2016.03.013.

[34] Bati SB, Fagone M, Rotunno T. Lower bound limit analysis of masonry arches with CFRP reinforcements: A numerical method. J Compos Constr 2013. https://doi.org/10.1061/(ASCE)CC.1943-5614.0000350.

[35] Bertolesi E, Milani G, Fedele R. Fast and reliable non-linear heterogeneous FE approach for the analysis of FRP-reinforced masonry arches. Compos Part B Eng 2016. https://doi.org/10.1016/j.compositesb.2015.11.005.

[36] Cancelliere I, Imbimbo M, Sacco E. Experimental tests and numerical modeling of reinforced masonry arches. Eng Struct 2010. https://doi.org/10.1016/j.engstruct.2009.12.005.

[37] Carozzi FG, Poggi C, Bertolesi E, Milani G. Ancient masonry arches and vaults strengthened with TRM, SRG and FRP composites: Experimental evaluation. Compos Struct 2018. https://doi.org/10.1016/j.compstruct.2017.12.075.

[38] Bertolesi E, Milani G, Carozzi FG, Poggi C. Ancient masonry arches and vaults strengthened with TRM, SRG and FRP composites: Numerical analyses. Compos Struct 2018. https://doi.org/10.1016/j.compstruct.2017.12.021.

[39] D’Ambrisi A, Feo L, Focacci F. Masonry arches strengthened with composite unbonded tendons. Compos Struct 2013. https://doi.org/10.1016/j.compstruct.2012.10.040.

[40] Foraboschi P. Strengthening of masonry arches with fiber-reinforced polymer strips. J Compos Constr 2004. https://doi.org/10.1061/(ASCE)1090-0268(2004)8:3(191).

[41] Valluzzi MR, Valdemarca M, Modena C. Behavior of brick masonry vaults strengthened by FRP laminates. J Compos Constr 2001. https://doi.org/10.1061/(ASCE)1090-0268(2001)5:3(163).

[42] Basilio I, Fedele R, Lourenço PB, Milani G. Assessment of curved FRP-reinforced masonry prisms: Experiments and modeling. Constr Build Mater 2014. https://doi.org/10.1016/j.conbuildmat.2013.11.011.

[43] Grande E, Milani G. Modeling of FRP-strengthened curved masonry specimens and proposal of a simple design formula. Compos Struct 2016;158. https://doi.org/10.1016/j.compstruct.2016.09.017.

[44] Bertolesi E, Milani G, Fagone M, Rotunno T, Grande E. Micro-mechanical FE numerical model for masonry curved pillars reinforced with FRP strips subjected to single lap shear tests. Compos Struct 2018;201:916–31. https://doi.org/10.1016/j.compstruct.2018.06.111.

[45] Bertolesi E, Fabbrocino F, Formisano A, Grande E, Milani G. FRP-Strengthening of Curved Masonry Structures: Local Bond Behavior and Global Response. vol. 747. 2017. https://doi.org/10.4028/www.scientific.net/kem.747.134.

[46] Rotunno T, Fagone M, Bertolesi E, Grande E, Milani G. Curved masonry pillars reinforced with anchored CFRP sheets: An experimental analysis. Compos Part B Eng 2019;174. https://doi.org/10.1016/j.compositesb.2019.107008.

[47] Malena M, de Felice G. Debonding of composites on a curved masonry substrate: Experimental results and analytical formulation. Compos Struct 2014;112:194–206. https://doi.org/10.1016/j.compstruct.2014.02.004.

[48] Grande E, Fagone M, Rotunno T, Bertolesi E, Milani G. Modelling of the bond behaviour of curved masonry specimens strengthened by CFRP with anchor spikes. Compos Part B Eng 2019;171:235–

45. https://doi.org/10.1016/j.compositesb.2019.04.027.

[49] Grande E, Fagone M, Rotunno T, Bertolesi E, Milani G. Coupled interface-based modelling approach for the numerical analysis of curved masonry specimens strengthened by CFRP. Compos Struct 2018. https://doi.org/10.1016/j.compstruct.2018.05.118.

[50] Fabbrocino F, Formisano A, Grande E, Milani G. Bond mechanism of FRPs externally applied to curved masonry structures: Experimental outcomes and numerical modeling. Key Eng. Mater., 2019. https://doi.org/10.4028/www.scientific.net/KEM.817.105.

[51] Rotunno T, Fagone M, Bertolesi E, Grande E, Milani G. Single lap shear tests of masonry curved pillars externally strengthened by CFRP strips. Compos Struct 2018. https://doi.org/10.1016/j.compstruct.2018.05.097.

[52] Bertolesi E, Milani G, Fagone M, Rotunno T, Grande E. Heterogeneous FE model for single lap shear tests on FRP reinforced masonry curved pillars with spike anchors. Constr Build Mater 2020. https://doi.org/10.1016/j.conbuildmat.2020.119629.

[53] Fagone M, Rotunno T, Xhemali A. The adhesion between CFRP sheet reinforcements and masonry arches: an experimental analysis. 2nd Int. Conf. Recent Adv. Nonlinear Model. – Des. Rehabil. Struct. CoRACC 2017, 2017, p. 112–20.

[54] Milani G, Grande E. Simple bisection procedure in quickly convergent explicit ODE solver to numerically analyze FRCM strengthening systems. Compos Part B Eng 2020. https://doi.org/10.1016/j.compositesb.2020.108322.